



Andreas Bramböck, BSc

# **Correlation of Bulk Properties and DEM Contact Models for Cohesive Powders**

## **MASTER'S THESIS**

to achieve the university degree of

Diplom-Ingenieur

Master's degree programme: Chemical and Process Engineering

Submitted to

**Graz University of Technology**

Supervisor

Univ.-Prof. Dipl.-Ing. Dr. techn. Johannes Khinast

Institute for Process and Particle Engineering

Co-Supervisor

Dipl.-Ing. Dipl.-Ing. Peter Loidolt

Institute for Process and Particle Engineering

Graz, December 2017

## ***AFFIDAVIT***

I declare that I have authored this thesis independently, that I have not used other than the declared sources/resources, and that I have explicitly indicated all material which has been quoted either literally or by content from the sources used. The text document uploaded to TUGRAZonline is identical to the present master's thesis.

---

Date

---

Signature

## ***Abstract***

In this thesis a calibration method is introduced to find proper model parameters for the Discrete Element Method (DEM) during powder simulations. The aim is to find appropriate contact models and to optimize them in that way to describe the flow behavior of different powders.

Therefore, the experimental determined flow behavior of different powders inside the FT4 rheometer is compared to the flow behavior in a DEM model of the FT4. The design of experiments (DOE) approach is used to get a functional relationship between the flow behavior and the contact model parameters. Consequently, the model parameters can be optimized to obtain the flow behaviors of different powders. The best possible precision of the calibration depends on the cohesion model and its ability to describe the flow behavior of a certain powder. The capability of different cohesion models is investigated to find the most feasible model. Starting from a reference cohesion model, different modifications are introduced and the new models are compared to the reference model. Three different powder types (free flowing, moderate cohesive and strong cohesive) are used as benchmark for the different contact models.

The calibration of the contact parameters without a cohesion model demonstrates the precision of the calibration method for simple contact models. The reference cohesion model can be used to describe free flowing powders. However, the improved models allow to model lower bulk densities and hence are more useful to model cohesive powders.

## ***Kurzfassung***

Diese Arbeit befasst sich mit der Kalibrierung angemessener Modell Parameter für die Diskrete Elemente Methode (DEM), welche für Pulversimulationen verwendet wird. Ziel ist es, die Anwendbarkeit verschiedene Kontaktmodelle zu vergleichen und diese bei Bedarf zu modifizieren um das Fließverhalten verschiedener Pulver beschreiben zu können.

Das FT4 Rheometer wird verwendet, um das Fließverhalten experimentell zu bestimmen. Dieses wird mit dem Fließverhalten einer DEM Simulation des FT4 Rheometer verglichen. Der verwendete Design of Experiments (DOE) Ansatz ermöglicht die Haupteinflüsse der verschiedenen Simulationsparameter auf das Fließverhalten zu evaluieren und dieses als Gleichung darzustellen. Somit kann das Fließverhalten der DEM Simulationen abgeschätzt werden. Im Umkehrschluss ermöglichen mehrere Gleichungen für verschiedene Rheometerversuche eine Optimierung der Eingabeparameter für ein bestimmtes Fließverhalten. Dabei bestimmt die Fähigkeit des verwendeten Modelles, verschiedene Fließverhalten zu beschreiben, die Genauigkeit dieser Optimierung. Durch die Kalibrierung verschiedener Kohäsionsmodelle kann die Anwendbarkeit dieser untersucht werden. Angefangen von einem bereits implementieren Referenzmodell, wird dieses modifiziert und die neuen Modelle mit dem Referenzmodell verglichen. Die Fließeigenschaften von drei verschiedene Pulverarten (freifließend, moderat kohäsiv und stark kohäsiv) werden als Anhaltspunkte für die Kalibrierung der Kontaktmodelle verwendet.

Die Kalibrierung der Kontakparameter ohne Kohäsionsmodell zeigt die Fähigkeit der Kalibrieremethode für einfache Kontaktmodelle. Das bestehende Referenzmodell kann freifließende Pulver gut darstellen, jedoch endet die Anwendbarkeit bei moderat kohäsiven Pulvern. Die Modifikation des Referenzmodelles ermöglicht das Fließverhalten moderat kohäsiver sowie auch stark kohäsiver Pulver zu beschreiben.

## ***Acknowledgment***

I would like to thank all who supported me during my thesis. I would like to give special thanks to Dipl.-Ing. Dipl.-Ing. Peter Loidolt, who instigated this work. Peter Loidolt was always interested in the progress of my work and gave me consummated support. He had not only a sympathetic ear for my problems in research and writing, but also reliable solutions. At this point, I would also like to thank the whole 'Loony Science Group'. Thanks to Univ.-Prof. Gernot Krammer and Ass.Prof. Stefan Radl to take their time for my examination. As well as I would like to thank Ass.Prof. Thomas Wallek, who takes over the chairman.

I would like to thank my whole family for the mental and of course financial support during my study. Who do not blame me for my rarely and often short stays at home.

At least I would like to thank Dipl. Ing. Dr. Daniel Treffer, who introduced me at the institute and Univ.-Prof. Johannes Khinast, who got me a job at the institute and allows me at this way to acquire experience in doing research in an inspiring working environment of ingenious scientists and technicians.

*“Science is like sex: sometimes something useful comes out, but that is not the reason we are doing it.” (Richard P. Feynman)*

## ***Table of Contents***

1.	Introduction .....	1
2.	Methods and Material .....	3
2.1.	Particle Contact Model .....	3
2.2.	Cohesion Models .....	4
3.	Contact Model Calibration.....	10
3.1.	Geometric Setup .....	10
3.2.	Rotational Shear Test .....	11
3.3.	Compressibility Test.....	13
3.4.	Wall Friction Test .....	14
3.5.	Method of Calibration.....	16
3.6.	Materials .....	18
4.	Results and Discussion .....	19
4.1.	Calibration of the SJKR2 model.....	20
4.2.	Calibration of the SJKR3 model.....	24
4.3.	Calibration of the SJKR Hysteresis model.....	28
4.4.	Calibration of the HVDW model.....	29
4.5.	Calibration of the HSF model .....	32
4.6.	Calibration without a cohesion model.....	32
4.7.	Prediction of Powder Flow .....	34
4.8.	Comparison with the materials used as benchmark .....	38
5.	Conclusions and Outlook .....	41
6.	References .....	42
7.	Table of Figures.....	44
8.	Appendix .....	46

## **1. Introduction**

Particles are an integral part of common fields in the industry. Their flow behavior influences many processes like powder flow from a hopper (Cleary & Sawley, 2002), blending (Alizadeh, Bertrand, & Chaouki, 2014), powder flow in a screw conveyer (Owen & Cleary, 2009) and many more. Particles are not only important for unit operations, but also whole manufacturing units like tableting (Furukawa et al., 2016), coating (Pei & Elliott, 2017) or the dosator process (Loidolt, Madlmeir, & Khinast, 2017) deal with the flow of particles. In the referenced work it is shown, that not only the particle properties, but also the process itself affects the flow behavior of powders. Consequentially, it is necessary to take a close look at the process and watch the particle flow during process optimization. One possible approach is to investigate the powder flow by means of numerical simulations. The discrete element method (DEM) (Cundall & Strack, 1979a) is often used for the simulation of powder. In DEM the motion of every single particle inside the powder bed is described based on the sum of all forces acting on the particle. In this work only the interaction forces between two particles in contact are considered. A contact law is needed to determine the interaction forces as a function of the virtual particle overlap. The contact law includes several model parameters which have to be calibrated by comparing the simulation results with the experimental results. For this reason, a calibration procedure is introduced in this work which uses the standardized experiments of a powder rheometer (FT4) for the model calibration. These standardized and often available experiments replace the experiments of the production process, which is more elaborate and often not available during the development of new processes. The powder rheometer uses different methods to measure flow behavior of powders. By considering several of these methods, shear properties as well as bulk properties are incorporated into the calibration. Therefore, these rheometer experiments have to be implemented in a DEM model. The open-source DEM software LIGGGHTS<sup>®</sup> (C. Kloss, Goniva, Hager, Amberger, & Pirker, 2012) is used for this purpose. The built-in Hertz model is used as contact model, which requires six model parameters to be defined. To reduce the calibration effort, the particle density as well as the Poisson's ratio are supposed to be constant. The material properties of lactose are used to define the particle density and the Poisson's ratio since lactose is a common excipient in pharmaceutical industry. By restricting ourselves to tight packed particles the particle rotation can be neglected. Hence the rolling friction coefficient is not considered in the calibration. Furthermore, numerical stability problems caused by the rolling friction model are avoided. A supplementary cohesive force

model improves the flow behavior to be more realistic for cohesive powders. LIGGGHTS<sup>®</sup> already includes several cohesion models for different applications. Nevertheless, the applicability to the FT4 experiments of different powders is limited. Therefore, existing cohesion models are improved and new cohesion models are implemented. According to the different cohesion models up to two additional parameters are included in the calibration. The calibration consists of two parts. Initially, the influence of each parameter is determined. A straightforward method is the design of experiments (DOE) approach, introduced by R. Fisher (Fisher, 1936). Basically DOE is used to find the impact of the influencing factors of experiments by doing a minimal number of experiments. DOE experiments are performed in a certain range of the influencing factors. The result of the experiments, called response, is used to derive a functional relationship between factors and responses, which can be used for predictions within the range of the factors. If DOE is applied to simulations, then the model parameters represent the influencing factors. Previous studies already used single FT4 rheometer experiments to calibrate DEM parameters (Å, Ketterhagen, & Hancock, 2010). In other studies DOE is applied as in (Wilkinson, Turnbull, Yan, Stitt, & Marigo, 2017) or to calibrate mixing in a paddle blade mixer in (Pantaleev, Yordanova, Janda, Marigo, & Ooi, 2017). The possibility to predict flow behavior based on given model parameters allows optimization of model parameters for known flow behavior. If the functional relationships of influencing factor and response of several different experiments is used, then the optimization can be improved.

The aim of this thesis is to investigate the capabilities of different cohesion models to describe cohesive flow behavior. Therefore, the flow behavior of three different types of powders is tested and taken as a reference. The described calibration method is used to optimize model parameters to predict the flow behavior of the reference powders.

## **2. Methods and Material**

The discrete element method used in this work is capable of computing mechanical behavior of assemblies of different particles. Frequently these particles are simply described as spheres. The computation of the particle acceleration, velocity and position is performed at fixed time steps. With Newton's second law the motion of the particles and therefore the position and velocity at the next time step, based on the forces acting on the particle, can be calculated. The maximum distance particles move during one time step has to be small compared to the particle diameter. The limitation of the time step is needed to follow the trajectories of the particles accurately. Due to the motion, particles may intersect and create an overlap. The force-displacement law gives the correlation between particle overlap and contact force. It is also known as contact model. The contact force is a main part of the force balance of Newton's second law. Other forces like gravity or cohesion may be also part of the force balance. (Cundall & Strack, 1979b).

There are many codes for DEM simulations. In our study the open source DEM software LIGGGHTS<sup>®</sup> (Kloss et al., 2012) is used.

### **2.1. Particle Contact Model**

To compute the contact force, the Hertz contact model (a standard model implemented in LIGGGHTS<sup>®</sup>) is used. The contact normal force  $F_n$  is a function of the effective Young's modulus  $E^*$ , the effective particle radius  $R^*$  and the particle normal overlap  $\delta_n$  as shown in Eq.(1). For the tangential contact force shown in Eq.(2), the effective shear modulus  $G^*$  and the tangential overlap  $\delta_t$  are additional input parameters. The Coulomb friction force limits the tangential contact force. It is a function of the coefficient of friction  $\mu_s$  and the contact normal force. The effective properties can be computed as a function of the particle diameter, Young's modulus and the Poisson's ratio of the two particles being in contact as it is shown in Eq. (3) to (5). Based on the coefficient of restitution  $e$ , damping forces in the normal and tangential directions were computed. This allows energy dissipation (equations not shown here). (Christoph Kloss, 2016).

$$F_n = \frac{4}{3} E^* \sqrt{R^*} \delta_n^{\frac{3}{2}} \quad (1)$$

$$F_t = \min \left\{ \begin{array}{l} 8G^* \sqrt{R^*} \delta_n \delta_t \\ \mu_s F_n \end{array} \right. \quad (2)$$

$$\frac{1}{E^*} = \frac{1 - \nu_1^2}{E_1} + \frac{1 - \nu_2^2}{E_2} \quad (3)$$

$$\frac{1}{R^*} = \frac{1}{R_1} + \frac{1}{R_2} \quad (4)$$

$$\frac{1}{G^*} = \frac{2(2 - \nu_1)(1 + \nu_1)}{E_1} + \frac{2(2 - \nu_2)(1 + \nu_2)}{E_2} \quad (5)$$

## 2.2. Cohesion Models

Additional to the contact force, cohesion forces influence the flow behavior. Basically, the cohesivity of powders depends on the ratio of the attractive cohesion forces between particles or particles and walls and the volume forces of the particles. The dimensionless granular Bond number  $Bo_g$  describes this ratio. It is defined as the ratio of surface forces and volume forces. In this work, it is defined as the ratio of contact cohesion force and particle gravity force (see Eq. (6)).

$$Bo = \frac{\text{surface force}}{\text{volume force}} = \frac{\text{cohesion force}}{\text{gravity force}} = \frac{F_c}{\frac{d^3 \pi \rho g}{6}} \quad (6)$$

For simple calibration simulations with the Hertz model six parameters are necessary. Since lactose is a very common excipient in pharmaceutical industry, the Poisson's ratio and the particle density are supposed to be constant at the material properties of lactose. Therefore, four parameters (particle diameter, Young's modulus, coefficient of friction and coefficient of restitution) must be defined. For simulations with cohesive powders, the number of parameters increases depending on the complexity of the cohesion model. In this work five different cohesion models are compared. Only one of them is already implemented in LIGGGHTS<sup>®</sup>, the other four are new models and had to be implemented.

### ***The modified simplified Johnson-Kendall-Roberts model (SJKR2)***

The SJKR2 model is already implemented in LIGGGHTS<sup>®</sup> (Christoph Kloss, 2016). The cohesion force is a linear function of a constant value, called the cohesion energy density  $cohE$  and the overlap area  $A_{cont}$  (Eq. (7) and Figure 1). Weakness of this model is that there is no cohesion force without an overlap. Slightly intersecting particles do almost have no cohesive attraction. The advantage of this model is the single additional parameter  $cohE$  compared to the simple Hertz model.

$$F_{coh} = cohE \cdot A_{cont} \quad (7)$$

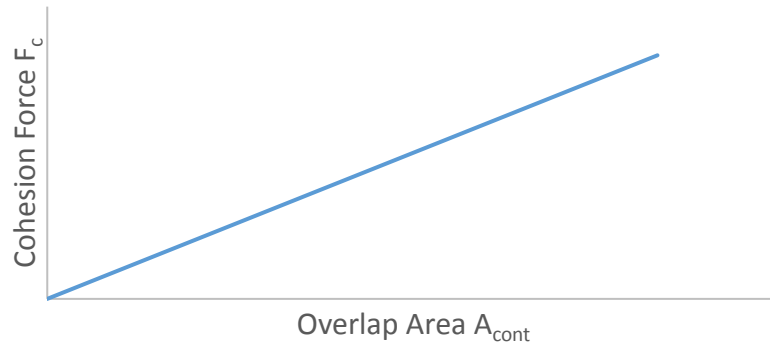


**Figure 1: Cohesion Force over Overlap Area for SJKR2 model**

### ***The modified simplified Johnson-Kendall-Roberts model with initial cohesion force (SJKR3)***

The SJKR3 model should overcome the weakness of the SJKR2 model by adding an initial cohesion force  $F_i$  (Eq. (8) and Figure 2). Just a slight intersect results in a cohesive attraction between two particles. It is useful to define the initial cohesion force by using the initial granular Bond number  $Bo_g$ . With the Bond number, a second additional cohesion parameter for the calibration occurs.

$$F_{coh} = cohE \cdot A_{cont} + F_i \quad (8)$$

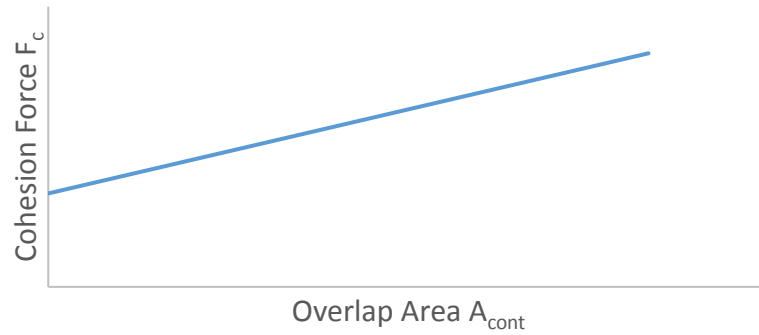


**Figure 2: Cohesion Force over Overlap Area for SJKR3 model**

### ***The modified simplified Johnson-Kendall-Roberts model with hysteresis (SJKR-HYS)***

To enable higher cohesion force after compaction, the hysteresis model was developed. In this model, the maximum overlap  $A_{max}$  is included in the calculation of the cohesion Force. At this way, higher cohesion attraction can be reached after the unloading path (Figure 3). The cohesion force at the unloading path is calculated based on a linear combination of the actual and the maximum contact area. The ratio of the contributions of the actual and the maximum contact area is given by

the ‘hysteresis factor’  $k_{hys}$  (Eq. (9) ). This factor results in a third cohesion parameter for the calibration.

$$F_{coh} = cohE \cdot (A_{cont} \cdot k_{hys} + A_{max} \cdot (1 - k_{hys})) + F_i \quad (9)$$

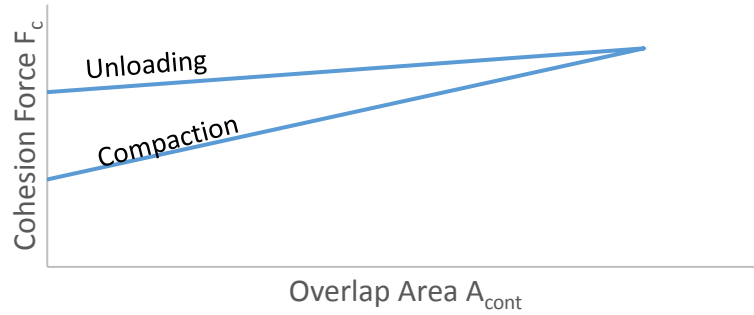


Figure 3: Cohesion Force over Overlap for SJKR-HYS model

### *The Hertzian Van-der-Waals model (HVDW)*

Frequently, the cohesion force is mainly attributed to the London-van der Waals force. Therefore, a modified version of the van der Waals force is implemented. The original form is shown at Eq. (10) and is derived by C. Hamaker (Hamaker, 1937). Originally, the force is acting between spheres with a certain distance  $D$  and the minimum distance is the atom spacing. This stands in contrast to the DEM, since the contact forces are computed as a function of an overlap. In the Hertzian van der Waals model the distance  $D$  is a fictional parameter because it is not measured as the distance of the particles in the simulation. Instead it is calculated as a function of the maximum Hertzian force during the contact history  $F_{b,max}$  (Eq. (11)) and can be seen at Figure

4. The advantage of this approach is, that the cohesion force is independent of the particle overlap. The particle overlap depends on the stiffness of the contact and every cohesion model which is based on the overlap is influenced by the contact stiffness. Hence, the Hertzian van der Waals model is supposed to be independent from the contact stiffness.

$$F_{vdw} = -\frac{A}{6D^2} \frac{R_1 R_2}{R_1 + R_2} \quad (10)$$

$$D = (D_{max} - D_{min}) \cdot \exp(-k F_{h,max}) + D_{min} \quad (11)$$

The Hamaker constant  $A$  is calculated at  $D_{max}$  to obtain a certain granular Bond number and is also a fictional parameter. The minimum distance  $D_{min}$  is fixed at 4 nm. The damping constant  $k$  and the Bond number are the two cohesion parameters of this model.

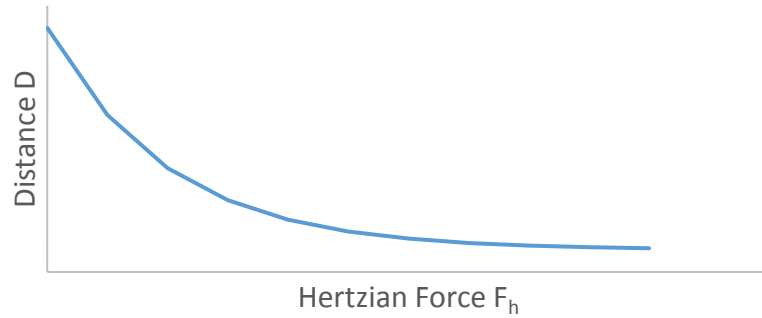


Figure 4: Distance function over Hertzian force for the HVDW model

### *The Hertzian saturated function model (HSF)*

Like in the HVDW model, the cohesion force is a function of the Hertzian force in the Hertzian saturated function model HSF. In the Hertzian saturated function model the cohesion force is directly calculated by the Hertzian force as a saturated function (Eq. (12) and Figure 5).

$$F_{coh} = (F_{max} - F_i) \cdot \left( 1 - \exp\left(-\frac{F_h}{F_g}\right) \right) + F_i \quad (12)$$

The maximal cohesion force  $F_{max}$  and the initial cohesion force  $F_i$  are calculated by maximum and initial granular Bond numbers. This two Bond numbers are the two cohesion parameters for calibration.

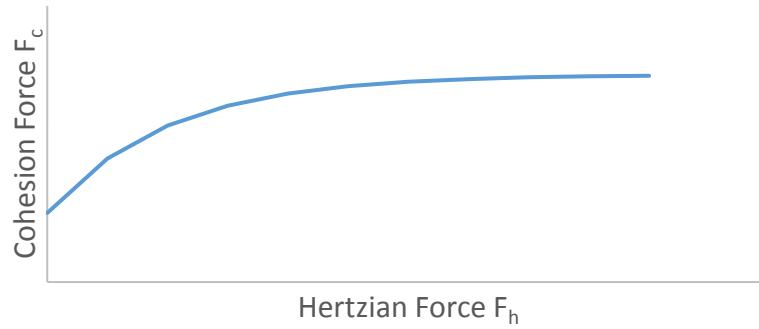


**Figure 5: Cohesion force over Hertzian force for HSF model**

### **3. Contact Model Calibration**

It is necessary to adjust the input parameters of the contact models properly to model the behavior of different powders. The process of finding the correct model parameters is called contact model calibration. In this work the calibration of the investigated contact models is based on the flow behavior of the powder. The experimental evaluation of the flow behavior is performed in a powder rheometer (FT4, from Freeman Technology). Specifically, the rotational shear test, the compressibility test and the wall friction test are used. These standard experiments are also implemented in LIGGGHTS<sup>c</sup> to compare the flow behavior of the powder in the simulation and the flow behavior of the real powder.

#### **3.1. Geometric Setup**

To recreate the FT4 experiments in the simulation the same geometry has to be used. All calibration simulations start with a filled vessel. The proportions of the receptacle are the same as in the real experiment. The only difference is the scale of the geometry in the simulation, since a smaller vessel is used in the simulation. The scale of the vessel is adjusted in that way to obtain same number of particles for different particle diameters. To guarantee a brimmed vessel more particles are settled than requested. An additional cylinder extends the height of the vessel and prevents loss of particles (see Figure 6). The excess particles are deleted. To avoid compaction of the powder bed caused by unrealistic high particle impact velocities, a viscous damping force is applied during particle settling. This damping force is equivalent to the drag force at a terminal velocity of 0.1 m/s.



**Figure 6: Filled vessel at FT4 experiment (left) and DEM simulation (right)**

Monodisperse particles may cause modeling artefacts like artificial regular arrangements of the particles. To avoid this, a mass based particle size distribution is introduced (see

Figure 7). The rather narrow distribution is used to avoid a high number of small particles and additional computational costs.

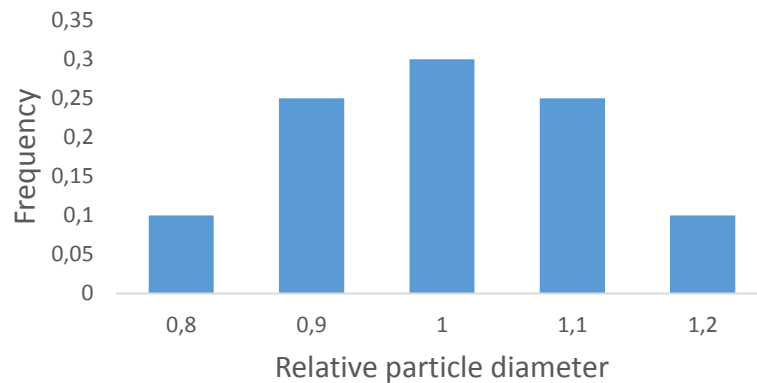


Figure 7: Particle size distribution

### ***3.2. Rotational Shear Test***

#### ***FT4 Experiment***

The main part of the experimental assembly is shown in Figure 9 left. The measuring instrument is the shear head. After preparing the sample, the automatic measuring program is started. The shear head compresses the powder by inducing a certain normal stress  $\sigma$ . Then a slow rotation of the shear head induces a shear stress  $\tau$  which is measured. The powder is compacted during this so-called pre-shearing step and therefore the shear stress increases. The rotation persists until the shear stress reaches a constant value. This is the pre-shear point. After pre-shearing, the yield point is measured. Therefore, a certain normal stress (which is lower than the pre-shear normal stress) is induced and the shear stress is increased until the powder starts to flow. The maximum shear stress is the yield point (Freeman, 2007). After replicating this measurement with different normal stresses during yielding, the yield points can be plotted in the  $\sigma$ - $\tau$  diagram. The fit through this points is the yield locus (shown in Figure 8). Every yield step is followed by a pre-shear step to get the same initial conditions. This means the yield locus describes the behavior of the powder after pre-shearing. The slope and the intercept of the yield locus are important flow parameters.

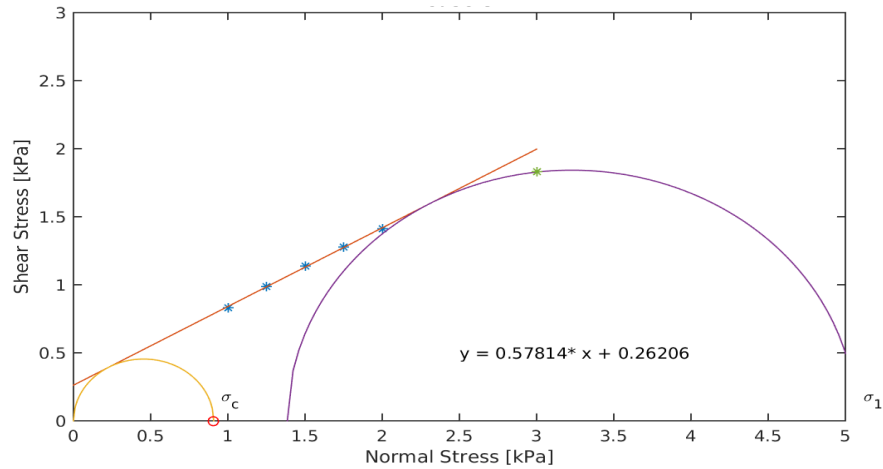


Figure 8: Plot of the Yield Locus fitted through the Yield points in the  $\sigma$ - $\tau$  diagram

### *Model of the Rotational Shear Test*

As in the shear cell experiment the simulation is split into the pre-shear and the yield step. In contrast to the experiment only one pre-shear simulation is needed which serves as starting point for different yield simulations. In Figure 9 the right picture shows the model of the shear cell module. The vessel moves upwards to adjust the normal stress  $\sigma$ . The shear head rotates for a certain duration and the shear stress  $\tau$  is measured during pre-shearing. Then the shear head is adjusted to remove the shear stress at a constant normal stress. At this point a restart file is created for subsequent yield simulations. This restart file contains the information of the position of all particles and the shear head. So the five yield simulations can be started with one restart file.

At the beginning of the yield simulation the vessel moves downwards to reduce the normal stress  $\sigma$ . The program adjusts the position of the vessel to maintain a certain normal stress. Then the shear momentum is slowly increased until the shear stress drops rapidly and the powder starts to flow (yield point). For each pre-shear simulation five yield simulations at different normal stresses are performed. The yield points are plotted and the linear fit through these five points is compared to the yield locus of the experiments.



Figure 9: Shear cell module of the FT4 rheometer (left) and model of the rotational shear test (right)

### 3.3. Compressibility Test

#### FT4 Experiment

The main part of the experimental assembly is shown in Figure 11. The measuring instrument is the compression head. After preparing the sample, the automatic measuring program is started. The tool moves downwards and induces a normal stress  $\sigma$ . At a predefined normal stress, the compression head stops and the traveling distance  $b$  is measured. The compressibility is the traveling distance divided by the initial height of the powder  $h_0$ . The compressibility as function of the normal stress is shown in Figure 10.

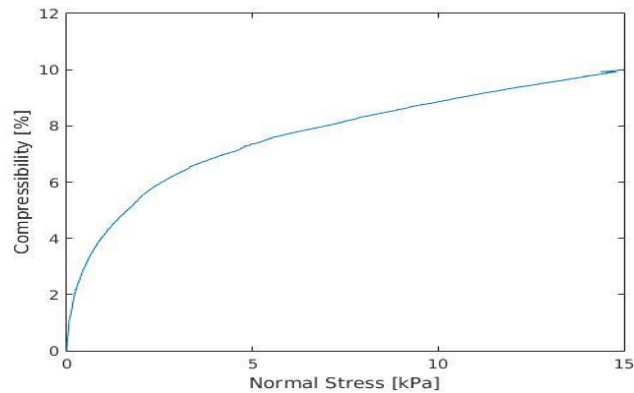


Figure 10: Compressibility over Normal stress

### ***Model of the Compressibility Test***

A data file of the filled but uncompressed vessel is used as starting point. A stamp moves downwards and compresses the powder. The normal stress  $\sigma$  and the traveling distance are recorded. At a certain defined normal stress, the stamp stops.



Figure 11: Compressibility module of the FT4 rheometer (left) and simulation of the compressibility testing (right)

### ***3.4. Wall Friction Test***

#### ***FT4 Experiment***

The wall friction test is similar to the pre-shear step during the rotational shear test. Instead of the shear head a plane metal or plastic head is used depending on which wall material is relevant for the industrial application of interest. The outcome of the experiment is the angle of wall friction which describes the friction between powder and the wall. After preparing the sample, the automatic measuring program is started. The measuring tool compresses the powder by inducing a certain normal stress  $\sigma$ . Then a slow rotation induces a shear stress  $\tau$ , which is measured. The measurement is repeated for different normal stresses and the tangential stress is plotted as function of the normal stress. Figure 12 shows the  $\sigma$ - $\tau$  diagram of the Wall Friction experiment. The slope of the fit is equivalent to the wall friction angle.

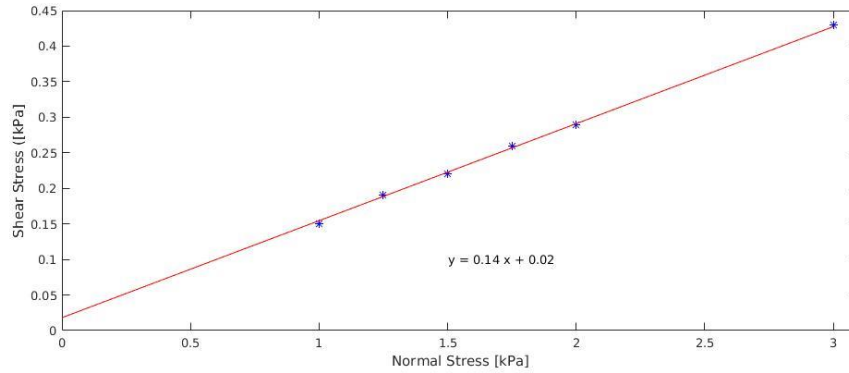


Figure 12:  $\sigma$ - $\tau$  diagram for the Wall Friction experiment.

### Model of the Wall Friction Test

The wall friction simulation is similar to the pre-shear simulation. The vessel moves upwards to adjust the normal stress  $\sigma$ . The stamp rotates a certain time and the shear stress  $\tau$  is measured. Then the stamp stops, the vessel moves downwards to adjust a lower normal stress and the stamp rotates again for a certain time. Figure 13 shows the curves of normal and shear stress over time. The constant shear stresses can be plotted over the normal stress. The slope of the linear fit through this points is the friction between particles and wall.

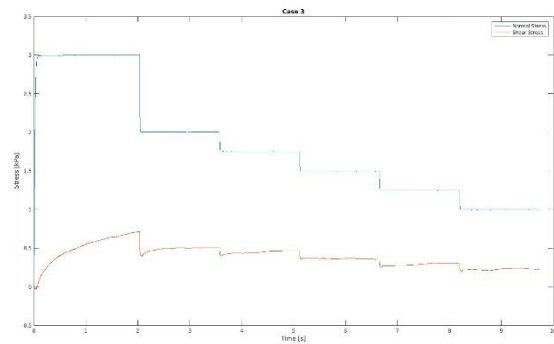
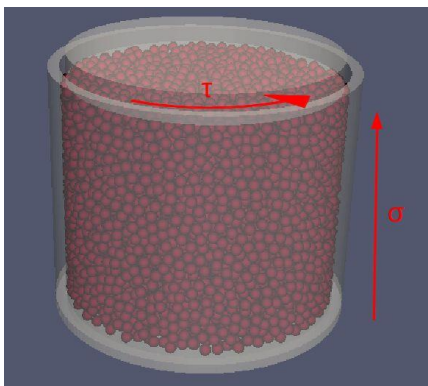


Figure 13: Simulation of the wall friction testing and stress over time diagram

### 3.5. Method of Calibration

The basic approach in the calibration method is to correlate the input parameter of the contact model and the flow behavior of the powder. If the functional relation of the model parameters and the powder properties is known, then the model parameters can be adjusted to obtain certain powder properties.

#### Design of Experiments (DOE)

The idea of DOE is to get the most information concerning the correlation between input (factor) and output (response) of experiments. The same approach can be used for black box simulations with many input parameters to minimize the computational effort. For each factor, an extreme high and low level is defined and both are used for simulations. The total number of required simulations is  $2^n$  where  $n$  is the number of factors.

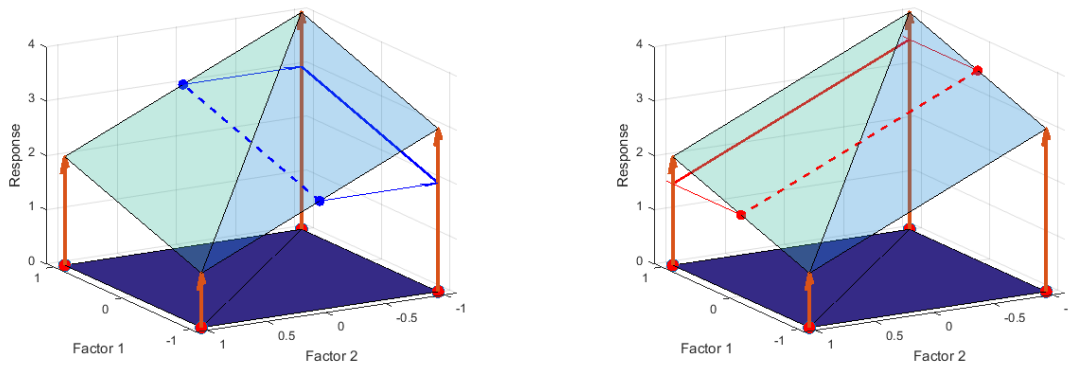


Figure 14: DoE example for two factors. Schematic view for the main effect of factor 1 (left) and factor 2 (right)

As shown in Figure 14, in case of two factors four extreme points must be evaluated. For each factor, the average response at the high and low level is calculated. The difference between the responses at high and low level gives the influence of the factor, also known as main effect. The main effects of the factors can be depicted in the main effects plot (Figure 15). The steeper the main effects plot is, the higher is the influence of the factor. And the flatter the plot, the lower is the influence of the factor. It is also possible to show the interaction between two factors. Therefore, the effect of a factor is plotted at two different levels of the second factor. In Figure 14 the edge

lines must be projected horizontally to obtain the two lines which indicate the influence of one factor at two different levels of the second factor. If the lines are not parallel, then the two factor interact with each other. This means the importance of the first factor changes if the second factor changes.

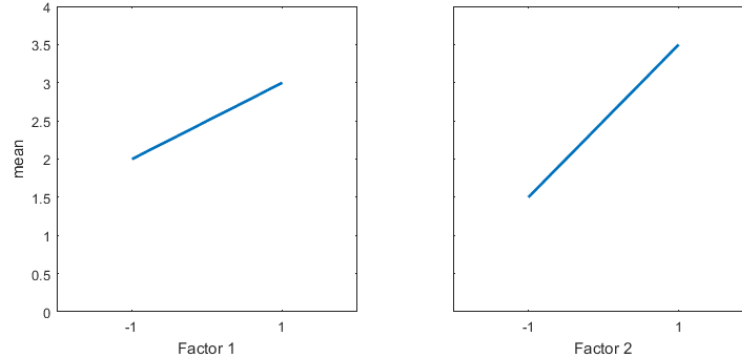


Figure 15: Maineffectsplot for a DoE with two factors

The slope of the maineffect is used to derive a function to predict the response as function of the factors. Eq. (13) shows the general form of this equation. It is a sum of the overall average  $c_0$ , the maineffects  $c_i$  times the value of factor  $i$  and the interaction between the two factors.

$$Response = c_0 + \sum_{i=1}^n c_i \cdot factor_i + \sum_{i=1}^n \sum_{j=i+1}^n c_{ij} \cdot factor_i \cdot factor_j \quad (13)$$

### *Prediction of Flow Behavior*

The application of the DOE concerning the simulation of the standard experiments yields few equations. Figure 16 shows the different factors and responses for the DEM simulations of the standard experiments. For every response one equation can be derived. Finally, one gets a minimum of four equations with at least five factors. The number of factors depends on the cohesion model. The main idea is, to predict the response by knowing the factors, it must be possible to get the factors by knowing the responses. The desired responses are obtained during FT4 experiments. It is not possible to invert the equations to determine the exact values of the contact parameters. However, it is possible to tune the factors in that way to match the desired responses as close as possible.



Figure 16: Factors and responses for the DEM simulations of the standard experiments

### 3.6. Materials

Three different cohesive powders are tested with the FT4 to give a range of meaningful simulation results. The aim is to describe all three types from the free flowing Lactohale 100 to the strong cohesive Lactohale 220. Table 1 lists the results of the FT4 experiments of the three powder types.

Table 1: Material properties: results from the standard experiments

	Compress.	Wall Fric. Angle	Pre-Shear Stress	Yield Locus
Lactohale 100	5.73%	7.77°	1.67 kPa	0.608 x + 0.14
Lactohale 200	21.52%	11.46°	2.16 kPa	0.668 x + 0.43
Lactohale 220	46.29%	20.03°	2.88 kPa	0.796 x + 0.88

## 4. Results and Discussion

In this chapter the results of the DOE simulations are discussed. In a first step the results of the different cohesion models are compared. For every cohesion model 17 simulations are needed (16 for the DOE to study the given ranges of the influencing factors and one for the middle point). The simulation of the middle point uses the average of each factor's range. If the middle point of the factors also yields a middle response, then the influence of the factor can be supposed to be linear. The span of the responses for each simulation set indicates the applicability of the model to describe different powder properties i.e. if the range of compressibility is high for a certain parameter set, then different powder types can be modeled with the same contact model. The responses are predicted based on the equations which give functional relationship of the factors and the responses. The relative prediction error is determined as difference of the prediction based on the response equations and the simulation result. Furthermore, the equations are used to adjust particular flow behavior to model a certain powder. Specifically, the simulation parameters are optimized to approximate the flow behavior of the materials described in chapter 3.6. The applicability of the prediction based on the response equations is compared to different cohesion models. An exemplary equation set for calibration without a cohesion model is shown in Eq. (14) - (17). In the equations the powder properties are described as function of the Young's Modulus (*Young*), the particle diameter (*dia*), the coefficient of friction (*mu*) and the coefficient of restitution (*e*).

$$\begin{aligned} \text{Preshearstress} = & 1.61 + 0.007 \cdot \text{Young} - 0.005 \cdot \text{dia} + 0.219 \cdot \text{mu} - 0.008 \cdot \text{e} + \\ & + 0.004 \cdot \text{Young} \cdot \text{mu} - 0.006 \cdot \text{Young} \cdot \text{e} - 0.002 \cdot \text{dia} \cdot \text{e} \end{aligned} \quad (14)$$

$$\begin{aligned} \text{Slope} = & 0.565 - 0.005 \cdot \text{Young} - 0.001 \cdot \text{dia} + 0.079 \cdot \text{mu} + 0.001 \cdot \text{e} - \\ & - 0.003 \cdot \text{Young} \cdot \text{mu} - 0.003 \cdot \text{Young} \cdot \text{e} - 0.001 \cdot \text{dia} \cdot \text{mu} \end{aligned} \quad (15)$$

$$\begin{aligned} \tau_0 = & 0.015 - 0.001 \cdot \text{Young} - 0.016 \cdot \text{dia} + 0.004 \cdot \text{m} - 0.001 \cdot \text{Young} \cdot \text{mu} + \\ & + 0.001 \cdot \text{Young} \cdot \text{e} - 0.003 \cdot \text{dia} \cdot \text{mu} - 0.002 \cdot \text{dia} \cdot \text{e} + 0.002 \cdot \text{mu} \cdot \text{e} \end{aligned} \quad (16)$$

$$\begin{aligned} \text{Compressibility} = & 3.57 - 0.35 \cdot \text{Young} - 0.08 \cdot \text{dia} - 0.07 \cdot \text{mu} - 0.06 \cdot \text{e} - \\ & - 0.01 \cdot \text{dia} \cdot \text{e} - 0.01 \cdot \text{mu} \cdot \text{e} \end{aligned} \quad (17)$$

The used DEM software LIGGGHTS<sup>®</sup> allows to define separate properties for contacts between particles and particle – wall contacts. In previous studies the relationship between the wall friction angle and the input parameters was investigated. It turns out, that the wall friction angle is indirectly correlated to the coefficient of friction for particle – wall contacts. Therefore, the integration of the wall friction testing in the calibration procedure is omitted.

#### **4.1. Calibration of the SJKR2 model**

Table 2 shows the range of the simulation parameters for the DOE. The simulation set includes five parameters. The cohesion energy density (*cohE*) is considered in addition to the parameters in the cohesionless model.

**Table 2: Range of the simulation parameter for the DOE simulation set using the SJKR2 cohesion model**

	Young	dia	cohE	mu	e
Low	20·10 <sup>6</sup> Pa	100·10 <sup>-6</sup> m	60 000 Jm <sup>-3</sup>	0.1	0.4
High	30· 10 <sup>6</sup> Pa	30010 <sup>-6</sup> m	90 000 Jm <sup>-3</sup>	0.15	0.8

The extreme values of the parameter range are used to define the simulation parameters for the simulation set. The DOE design is shown in the Appendix (A 1), where -1 substitutes the lower value and 1 the upper value. The results of all simulations are shown in A 2, however the span of the responses is of main interest. Table 3 shows the minimum and the maximum response of the simulation set for all calibration methods. The rotational shear testing (pre-shear stress, yield locus) yields comparable values for free flowing and moderate cohesive powders (compare Table 1). But the response of the compressibility is only applicable for free flowing powders. The low compressibility results from the high bulk density of the initial powder packing. This may be due to the characteristics of the contact model. In the SJKR2 model the cohesion force is proportional to the overlap. During filling of the vessel only slight overlaps occur, and therefore the cohesion forces are low. As a consequence the particles pack very dense and high bulk densities are achieved.

**Table 3: Range of the responses for the different calibration methods and the prediction error using the SJKR2 cohesion model**

	Lower Limit	Upper Limit	Prediction Error
Pre-Shear Stress	1.55 kPa	2.36 kPa	0.7%
Slope of Yield Locus	0.515	0.737	2.9 %
$\tau_0$ of Yield Locus	0.08	0.38	3.0%
Compressibility	3.08 %	4.34 %	1.4%

The results of the simulations are also used to derive response equations. These equations are used to predict the response for a certain set of influencing factors (see A 2). A relative prediction error is calculated and shown in Table 3. The equations predict the responses quite accurately for all calibration methods. The isolated effect of each influencing parameter is displayed in the main effects plot. The main effects plot for the pre-shear stress is presented in Figure 17. The most important influencing factor is the coefficient of friction. The higher  $\mu$  is, the higher is the pre-shear stress. The pre-shear procedure is a continuous shear process at a certain normal stress. In this process the particles are pressed towards each other based on the externally applied normal stress. During pre-shearing the particles have to slide on each other despite the compression force. Therefore, friction forces between the particles are the main source for the resistance of the powder against shear. The compression forces cause overlaps of the particles and inducing cohesion forces which enhance the normal forces. As a consequence, the cohesion energy density has a small influence on the pre-shearing stress. Contrary, the higher the Young's modulus, the smaller is the overlap and thereby the influence of the cohesive force. The particle diameter as well as the coefficient of restitution only slightly influence the pre-shear stress.

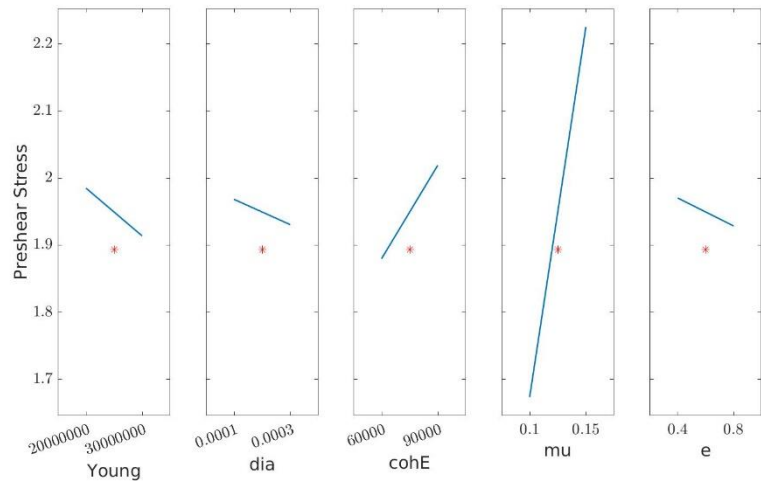


Figure 17: Main effects plot for the Pre-Shear Stress using the SJKR2 cohesion model

The main effects plot for the slope of the yield locus is shown in Figure 18. The slope of the yield locus corresponds to the internal friction of the powder. Consequently, the main effects plot of the slope of the yield locus is similar to the main effects plot of the pre-shear stress. The center point of the main effects plot does not lie on the line in between of the extreme values of the responses indicating an inexact prediction of the response. If narrower ranges for the coefficient of friction are used then a more central middle point might be achieved. However, a deviation of 4% is within a sufficient precision.

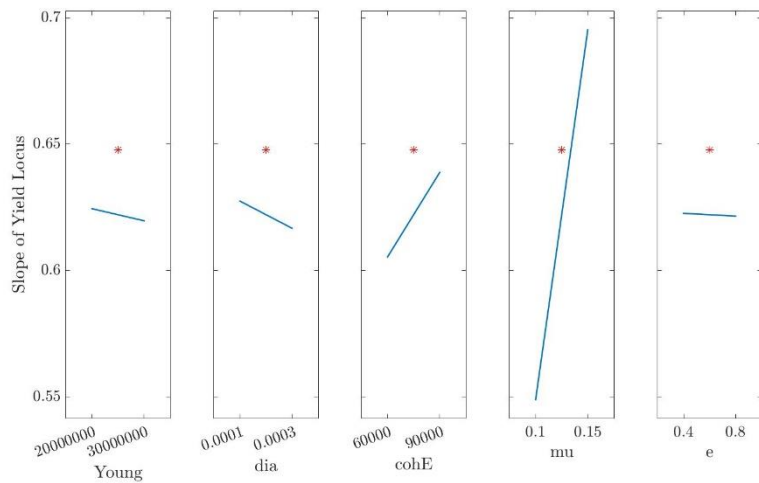


Figure 18: Main effects plot for the Slope of the Yield Locus using the SJKR2 cohesion model

The intercept of the yield locus  $\tau_0$  is an indicator for the flowability of the powder. For powders with higher  $\tau_0$ , it is more difficult, to get the bulk solid to flow. The origin of this behavior lies in particles which stick to each other without external forces. The cohesion forces enhance the maximum friction forces and therefore the resistance against shearing increases. The influences of all simulation parameters are shown in Figure 19. The cohesion force between particles is more distinct for higher cohesion energy densities. Thus the cohesion energy density as well as the coefficient of friction are the main influencing factors for the intercept of the yield locus. A lower Young's modulus causes a larger overlap and therefore the cohesion force and the resistance against flow increases. The smaller the diameter, the larger is the influence of the surface forces, like the cohesion force, compared to the other forces.

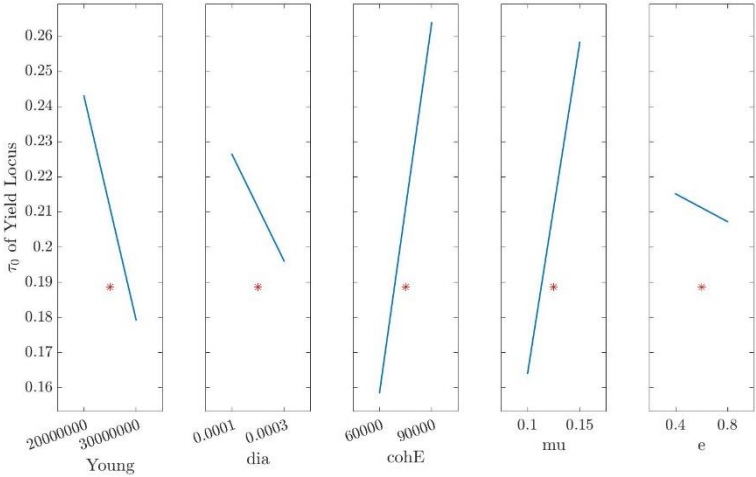


Figure 19: Main effects plot for the  $\tau_0$  of the Yield Locus using the SJKR2 cohesion model

The compressibility is an essential measure of the initial bulk density. Powders with high bulk densities are obviously harder to compress further than powders of loose packed particles. With the SJKR2 model only dense packed powder beds are obtained. In case of dense packed powders, particles are not able to rearrange and to increase the packing density, but they have to be pressed together. Therefore, the most important influencing factor is the Young's modulus (see Figure 20). A lower Young's modulus allows a higher overlap since particles can be pressed together more easily.

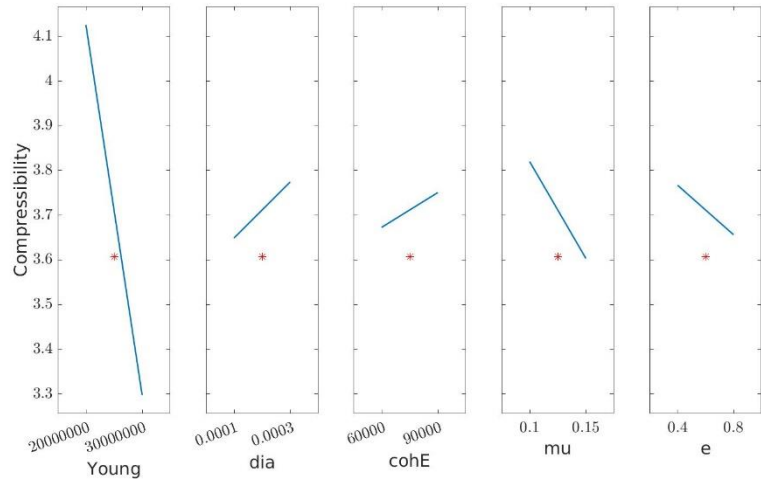


Figure 20: Main effects plot for the compressibility using the SJKR2 cohesion model

#### 4.2. Calibration of the SJKR3 model

Table 4 shows the range of the simulation parameters of the SJKR3 model which is investigated in the DOE. The simulation set includes six parameters. In addition to the five parameters used for the calibration of the SJKR2 model, the granular Bond Number  $B_0$  is introduced.

Table 4: Range of the simulation parameter for the DOE simulation set using the SJKR3 cohesion model

	Young	dia	Bo	cohE	mu	e
Low	$20 \cdot 10^6$ Pa	$100 \cdot 10^{-6}$ m	2 000	5 000	0.1	0.4
High	$30 \cdot 10^6$ Pa	$300 \cdot 10^{-6}$ m	8 000	10 000	0.15	0.8

The DOE design used for the calibration of the SJKR3 model as well as the results of the simulations are shown in the Appendix (A 3, A 4). The enhancement of the SJKR3 model compared to the SJKR2 model is the constant initial cohesion force, calculated with the granular Bond number. In comparison to the results based on the SJKR2 cohesion model, the range of  $\tau_0$  and the compressibility are raised and it is possible to describe strong cohesive powders (see Table 5). On the contrary, the upper limits of the pre-shear stress and the slope of the yield locus are lowered. The compressibility of free flowing powders cannot be reached, since the high Bond numbers used

in the study cause low packing densities of the powder beds. The prediction errors are good, however, a narrower range of the Bond number may improve the linearity and the precision of the prediction.

**Table 5: Range of the results for the different calibration methods and the prediction error using the SJKR3 cohesion model**

	Lower Limit	Upper Limit	Prediction Error
Pre-Shear Stress	1.42 kPa	1.91 kPa	2.2%
Slope of Yield Locus	0.293	0.612	10.8 %
$\tau_0$ of Yield Locus	0.13	1.03	14.4%
Compressibility	28.37 %	67.07 %	1.4%

The main influences of the pre-shear testing are similar to the SJKR2 cohesion model and are shown in the Appendix (A 5). Contrary to the cohesion energy density, the initial cohesion force is not dependent on the overlap of the particles. An increasing Bond number and the resulting higher initial cohesion force causes a lower slope of the yield locus (see Figure 21). The influence of the particle diameter results from the calculation of the initial cohesion force, which is scaled by the particle diameter. The coefficient of friction influences the slope similar as during the calibration of the SJKR2 cohesion model.

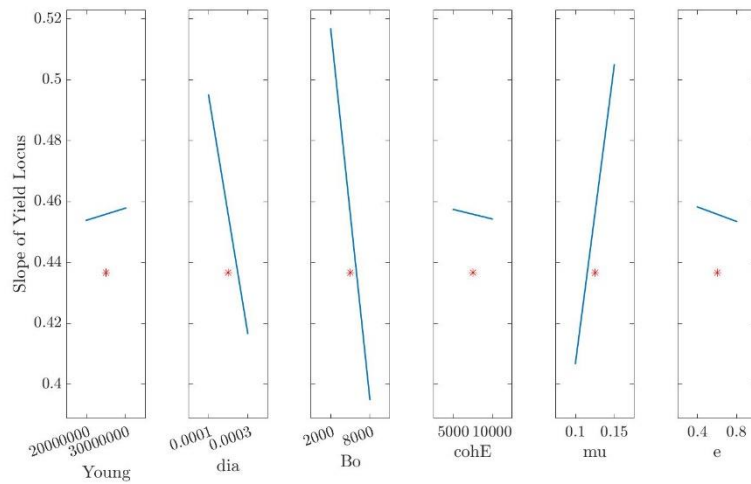


**Figure 21: Main effects plot for the slope of the yield locus using the SJKR3 cohesion model**

In comparison to the SJKR2 cohesion model, the main influence on the intercept of the yield locus has the Bond number (see Figure 22). The influence of the initial cohesion force is higher than the influence of the cohesion energy density, since no overlap is needed to create a cohesion force. The influence of the diameter is similar as it is for the slope of the yield locus. The influence of the coefficient of friction is the same as described in the calibration with the SJKR2 cohesion model. The main effects of the influencing factors of the pre-shear stress, the slope of the yield locus and the intercept of the yield locus have to be discussed together. The pre-shear point is mainly determined by the coefficient of friction since particles are externally compressed to each other. In this case the cohesion forces are of minor importance. Contrary, the intercept of the yield locus is mainly influenced by the cohesion force since the externally pressure is zero. In this way, a lower slope of the yield locus is observed for higher cohesion forces.

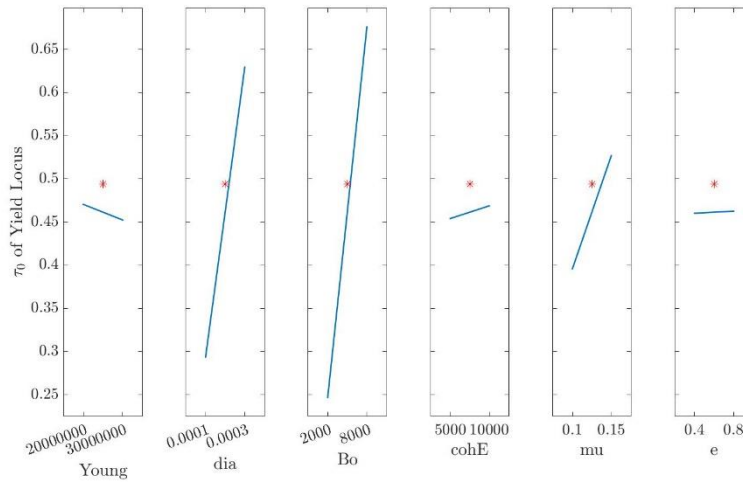


Figure 22: Main effects plot for the  $\tau_0$  of the Yield Locus using the SJKR3 cohesion model

The main effects plot of the compressibility for the SJKR3 model is shown in Figure 23. The influence of the Young's modulus can be neglected in this case, since particles are initially loose packed. The main influence has the particle diameter. The smaller the particles, the higher is the influence of the cohesive force to the particles. As well a higher Bond number causes a higher cohesive force and the cohesive force effects the initial bulk density.

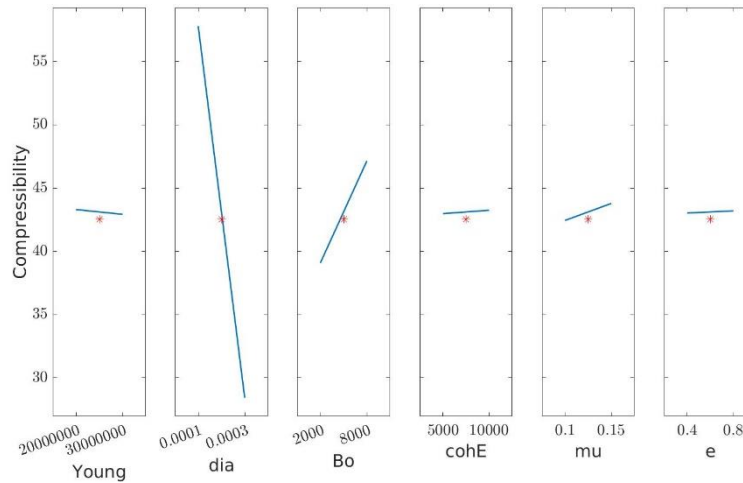


Figure 23: Main effects plot for the compressibility using the SJKR3 cohesion model

### 4.3. Calibration of the SJKR Hysteresis model

Table 6 shows the range of the simulation parameters considered in the DOE of the SJKR hysteresis model. The simulation set includes six parameters. The calibration of the SJKR3 cohesion model already showed the neglectable influence of the coefficient of restitution. To reduce the simulation effort, the hysteresis factor *hysfac* is used during the calibration and the coefficient of restitution is omitted.

**Table 6: Range of the simulation parameter for the DOE simulation set using the SJKR Hysteresis cohesion model**

	Young	dia	Bo	cohE	mu	hysfac
Low	$20 \cdot 10^6$ Pa	$100 \cdot 10^{-6}$ m	2 000	5 000	0.1	0.6
High	$30 \cdot 10^6$ Pa	$300 \cdot 10^{-6}$ m	8 000	10 000	0.15	0.8

The employed DOE design is shown in A 6. The result of the calibration of the SJKR Hysteresis model are compared in Table 7. Contrary to the expectations, the results are similar to the SJKR2 cohesion model and not to the SJKR3 cohesion model. The SJKR Hysteresis cohesion model is not able to describe cohesive particle flow. The Hysteresis model is a history based cohesion model. The cohesion force is calculated using the maximum overlap in contact history. Since the implementation of history based cohesion models is not that simple it seems, the cohesive force is calculated in a wrong way. If the maximum overlap is not used in the calculation, a higher overlap results a lower cohesive force. Therefore, the intercept of the yield locus describes a non-cohesive behavior, while the compressibility rises compared to the SJKR2 cohesion model.

**Table 7: Range of the results for the different calibration methods and the prediction error using the SJKR Hysteresis cohesion model**

	Lower Limit	Upper Limit	Prediction Error
Pre-Shear Stress	1.37 kPa	1.88 kPa	2.4%
Slope of Yield Locus	0.473	0.664	3.2 %
$\tau_0$ of Yield Locus	-0.02	0.04	844.9%
Compressibility	3.34 %	8.91 %	28.6%

All results as well as the main effects plots are similar to the SJKR2 cohesion model and shown in the Appendix. (A 7 - A 11)

#### ***4.4. Calibration of the HVDW model***

The HVDW cohesion model is quite different to the other ones. The cohesion force not depends on the overlap. Therefore, the cohesion energy density is replaced by the distance function coefficient  $dfc$ . The calibration ranges are shown in Table 8. Since previous simulations show the neglectable influence of the coefficient of restitution  $e$ , this factor is omitted.

**Table 8: Range of the simulation parameter for the DOE simulation set using the HVDW cohesion model**

	Young	dia	Bo	mu	dfc
Low	$20 \cdot 10^6$ Pa	$100 \cdot 10^{-6}$ m	3 000	0.1	$2 \cdot 10^4$
High	$30 \cdot 10^6$ Pa	$300 \cdot 10^{-6}$ m	8 000	0.15	$5 \cdot 10^4$

The span of the results is wide and the prediction error acceptable (see Table 9). The model reaches a high pre-shear stresses and a high intercept, which describes strong cohesive powders. In

contrast the slope of the yield locus and the compressibility are in ranges of free flowing powders. The low slope of the yield locus is reasoned by the high influence of  $dfc$ . The HVDW cohesion model is also a history based cohesion model. The calculation of the cohesion force is different to the SJKR Hysteresis model. The cohesion force is influenced by the maximum Hertz force. Since the history based implementation shows some troubles, the initial cohesive forces are too low and the compressibility of cohesive powders cannot be reached.

**Table 9: Range of the results for the different calibration methods and the prediction error using the HVDW cohesion model**

	Lower Limit	Upper Limit	Prediction Error
Pre-Shear Stress	1.37 kPa	4.42 kPa	17.3 %
Slope of Yield Locus	0.214	0.673	15.1 %
$\tau_0$ of Yield Locus	0.00	1.99	19.1%
Compressibility	3.73 %	10.65 %	13.8%

Figure 24 shows the main effects plot of the pre-shear stress using the HVDW cohesion model. In contrast to previous calibrations, not only the coefficient of friction influences the pre-shear stress. The higher the Hertz force is, the higher is the cohesion force. The diameter, the granular Bond number and the distance function coefficient are important for the calculation of the cohesion force. The shear force, the Hertz force and also the cohesion force amplify each other. That generates more resistance against shearing. A low  $dfc$  is equivalent to a high cohesive force.

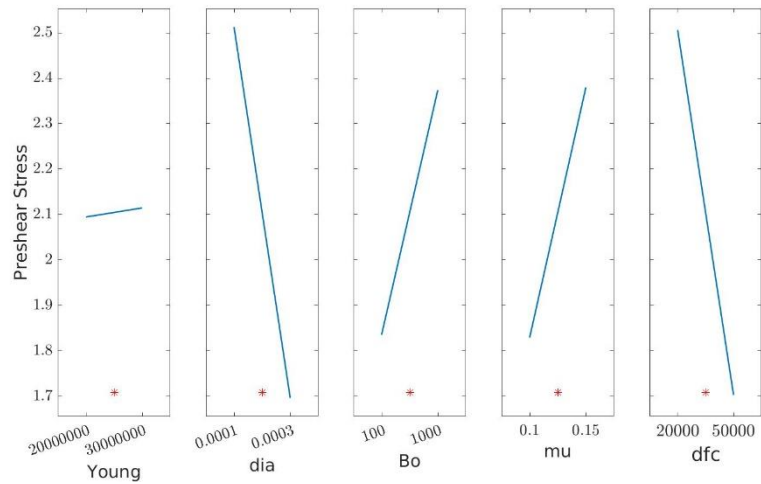


Figure 24: Main effects plot for the Pre-Shear Stress using the HVDW cohesion model

The main effects plots of the yield locus are in the Appendix (A 14 - A 15). The influence of the factors is similar to the SJKR3 cohesion model. A high cohesion force results a low slope of the yield locus and a high intercept of the yield locus. Figure 25 shows the main effects plot of the compressibility using the HVDW cohesion model. The influence of the Young's Modulus and the granular Bond number is similar to previous calibrations. The contrary influence of particle diameter and the distance function coefficient is probably a result of the problematic history based implementation of the cohesion model.

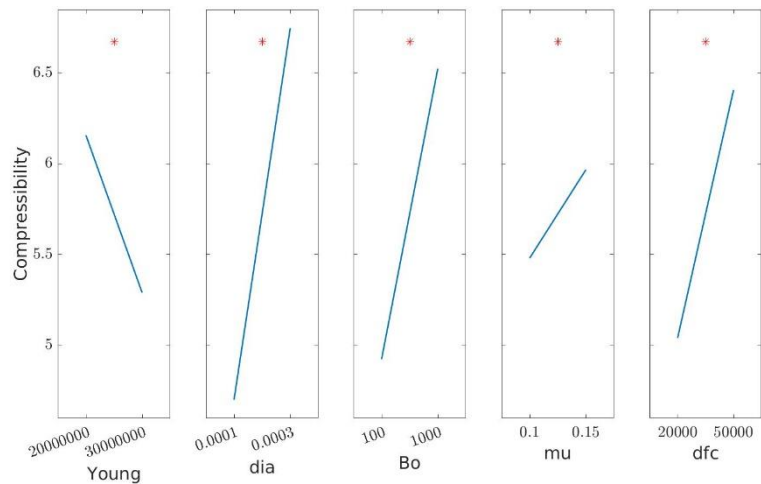


Figure 25: Main effects plot for the compressibility using the HVDW cohesion model

#### 4.5. Calibration of the HSF model

Due to the difficulties arisen in previous calibrations of history based cohesion models. The calibration of the HSF cohesion model is omitted.

#### 4.6. Calibration without a cohesion model

Table 10 shows the range of the simulation parameters for the DOE. The simulation set includes four parameters. The Youngs' Modulus (*Young*), the particle diameter (*dia*), the coefficient of friction (*mu*) and the coefficient of restitution (*e*).

Table 10: DOE ranges for the calibration without cohesion

	Young	dia	mu	e
Low	$20 \cdot 10^6$ Pa	$100 \cdot 10^{-6}$ m	0.1	0.4
High	$30 \cdot 10^6$ Pa	$300 \cdot 10^{-6}$ m	0.15	0.8

The results (shown in

Table 11) display shear properties of a free flowing powder without any cohesion forces. The compressibility is low and the intercept of the yield locus  $\tau_0$  is close to zero. The prediction errors are small, except for the prediction of the intercept. However, the prediction in the range of almost zero is not relevant. All results are summed up in the Appendix (A 17). The main influencing factors for calibration without a cohesion model are very similar to the calibration using the SJKR2 cohesion model, but without the cohesion energy density. The main effect plots are shown in the Appendix (A 18 - A 21). The influence of the particle diameter on the intercept of the yield locus can be neglected at this low values.

**Table 11: Range of the results for the different calibration methods and the prediction error**

	Lower Limit	Upper Limit	Prediction Error
Pre-Shear Stress	1.36 kPa	1.91 kPa	3.0%
Slope of Yield Locus	0.468	0.666	4.7 %
$\tau_0$ of Yield Locus	-0.01	0.07	194.4%
Compressibility	3.04 %	4.16 %	1.1%

#### ***4.7.Prediction of Powder Flow***

The previous calibrations show the scope of the different cohesion models. In this chapter the calibrated equations are used to get appropriate model parameters to predict a certain flow behavior within this area of application. Depending on the cohesion model, the values of flow behavior may be achieved in different precisions. Therefore, the flow behavior of three different materials are used as bench mark and not as fixed value. The assessment of the calibration of the different cohesion models is based on the predicted values and not on the flowability of the reference material.

##### ***Prediction without a cohesion model***

The calibration without using a cohesion model acts as a reference for the other calibrations and shows the possibilities of the calibration method. Table 12 displays the model parameter used for prediction Table 12.

Table 12: Optimized simulation parameters inspired by the defined materials without a cohesion model

	Young	dia	mu	e
Lactohale 100	$28.9 \cdot 10^6$ Pa	$171 \cdot 10^{-6}$ m	0.134	0.71
Lactohale 200	$30.0 \cdot 10^6$ Pa	$106 \cdot 10^{-6}$ m	0.150	0.42

The prediction based on the strong cohesive powder Lactohale 220 is omitted, since the prediction of the strong cohesive powders is not in an adequate precision. Table 13 compares the simulation results with the predicted values of two types of powders. The variation of the predicted values compared to the reference flow behavior depends on the area of application of the contact model. However, the simulated flowability is in a really good precision compared to the predicted flow behavior. The functionality of the calibration method is proven for a simple contact model.

**Table 13: Comparison of predicted and simulated flow behavior without using a cohesion model**

	Lactohale 100		Lactohale 200	
	Predicted	Simulated	Predicted	Simulated
Pre-Shear Stress	1.69 kPa	1.68 kPa	1.85 kPa	1.86 kPa
Slope of Yield Locus	0.588	0.588	0.640	0.631
$\tau_0$ of Yield Locus	0.02	0.02	0.03	0.05
Compressibility	3.21 %	3.23 %	3.13 %	3.16 %

***Prediction using the SJKR2 cohesion model***

Using the SJKR2 cohesion model a fifth parameter is used for calibration. Table 14 shows the used contact parameters for predicting flow behavior based on the reference materials. It can be seen that only the particle diameter and the coefficient of friction is changing.

**Table 14: Optimized simulation parameters inspired by the defined materials using the SJKR2 cohesion model**

	Young	dia	cohE	mu	e
Lactohale 100	$30.0 \cdot 10^6$ Pa	$170 \cdot 10^{-6}$ m	61 300	0.11	0.79
Lactohale 200	$30.0 \cdot 10^6$ Pa	$100 \cdot 10^{-6}$ m	61 900	0.15	0.79

Table 15 compares the prediction with the simulation result for two different powder types. The flow behavior of the free flowing powder Lactohale 100 is reproduced in a decent precision. Only the pre-shear stress is low compared to the prediction. The prediction of the flow behavior based on the moderate cohesive powder Lactohale 200 is also in really good precision. However, the intercept of the yield locus as well as the compressibility are too low. Based on the cohesion model, the initial bulk density as well as the compressibility cannot be increased. The cohesion

model also disables a higher intercept of the yield locus. The moderate simulation of Lactohale 200. The prediction in reference to a strong cohesive powder is omitted.

**Table 15: Comparison of predicted and simulated flow behavior using the SJKR2 cohesion model**

	Lactohale 100		Lactohale 200	
	Predicted	Simulated	Predicted	Simulated
Pre-Shear Stress	1.71 kPa	1.49 kPa	2.19 kPa	2.19 kPa
Slope of Yield Locus	0.576	0.609	0.675	0.689
$\tau_0$ of Yield Locus	0.12	0.14	0.21	0.20
Compressibility	3.25 %	3.22 %	3.04 %	3.01 %

***Prediction using the SJKR3 cohesion model***

Table 16 shows the optimized simulation parameters using the calibration of the SJKR3 cohesion model. The calibration limits the maximal pre-shear stress. Therefore, the maximum value of the coefficient of friction is increased. The coefficient of friction is extrapolated. Also the granular Bond number increases with stronger cohesive behavior.

**Table 16: Optimized simulation parameters inspired by the defined materials using the SJKR3 cohesion model**

	Young	dia	Bo	cohE	mu	e
Lactohale 100	$20 \cdot 10^6$ Pa	$250 \cdot 10^{-6}$ m	500	5 000	0.1	0.4
Lactohale 200	$20 \cdot 10^6$ Pa	$300 \cdot 10^{-6}$ m	2 750	5 000	0.2	0.4
Lactohale 220	$20 \cdot 10^6$ Pa	$300 \cdot 10^{-6}$ m	5 000	5 000	0.28	0.4

Table 17 compares the prediction resulting from the calibration and the simulated results for the three different powder types. The flow behavior prediction of the free flowing powder is hardly possible. The shear properties are too low and the compressibility is oversized. However, the flow behavior of a moderate cohesive powder is appropriate. The simulation results are in a good precision to the predicted values and the range of the flow behavior correspond to the flow behavior of the reference materials. The modified SJKR3 cohesion model allows to simulate strongly cohesive powders. The pre-shear stress as well as the slope of the yield locus is limited by the maximum value of coefficient of friction, but the intercept of the yield locus and the compressibility are in accordance to the reference material Lactohale 220.

**Table 17: Comparison of predicted and simulated flow behavior using the SJKR2 cohesion model**

	Lactohale 100		Lactohale 200		Lactohale 220	
	Predicted	Simulated	Predicted	Simulated	Predicted	Simulated
Pre-Shear Stress	1.67 kPa	1.61 kPa	2.08 kPa	2.31 kPa	2.57 kPa	2.66 kPa
Slope of Yield Locus	0.571	0.535	0.694	0.667	0.793	0.655
$\tau_0$ of Yield Locus	0.17	0.09	0.42	0.61	0.91	1.13
Compressibility	26.36 %	29.03 %	40.26 %	54.24 %	53.99 %	57.89 %

#### 4.8. Comparison with the materials used as benchmark

In this chapter the predicted Powder flow is compared to the materials defined in chapter 3.6. Figure 26 compares the flow behavior of Lactohale 100 with the flow behavior predicted by the different cohesion models. The flow behavior of all cohesion models are appropriate for the pre-shear stress and the slope of the yield locus. Without cohesion, the intercept of the yield locus and the compressibility cannot be reached. Contrary the SJKR2 cohesion model describes the intercept of the yield locus very well. The compressibility is also at a very low level, but for a free flowing powder like Lactohale 100 it is sufficient accurate. The flow behavior using the SJKR3 cohesion model describes the benchmark very well. The compressibility is too high, but a new calibration with lower granular Bond numbers will allow an accurate compressibility.

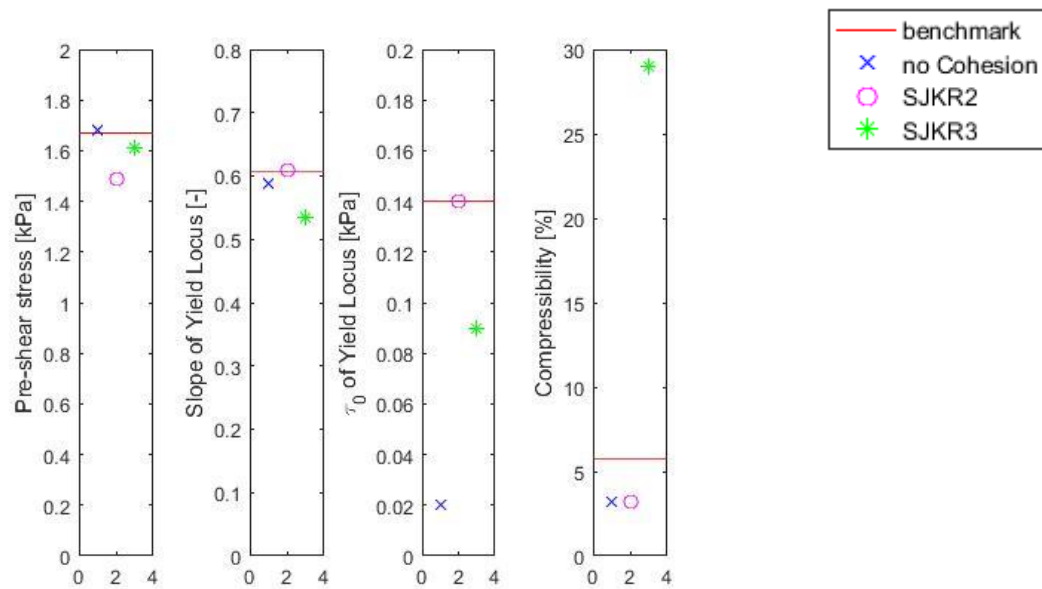


Figure 26: Comparison of the flow behavior of different cohesion models to the flow behavior of Lactohale 100 used as benchmark

The comparison of the different cohesion models using the moderate cohesive Powder Lactohale 200 as benchmark is shown in Figure 27. The applicability of the prediction without a cohesion model ends with free flowing powders. The pre-shear stress as well as the slope of the yield locus is in a sufficient precision, but the level of the values are more like a free flowing powder.

The intercept of the yield locus and the compressibility are similar to the prediction of the flow behavior of Lactohale 100. The SJKR2 cohesion model predicts the flow behavior very well. The prediction of the pre-shear stress and the slope of the yield locus is very accurate. The prediction of the intercept of the yield locus is a tad small. The compressibility is similar to the prediction of Lactohale 100. The results using the SJKR3 cohesion model describe a more cohesive flow behavior. The pre-shear stress and slope of the intercept are in a very accurate. The intercept and the compressibility is the range of strong cohesive powders.

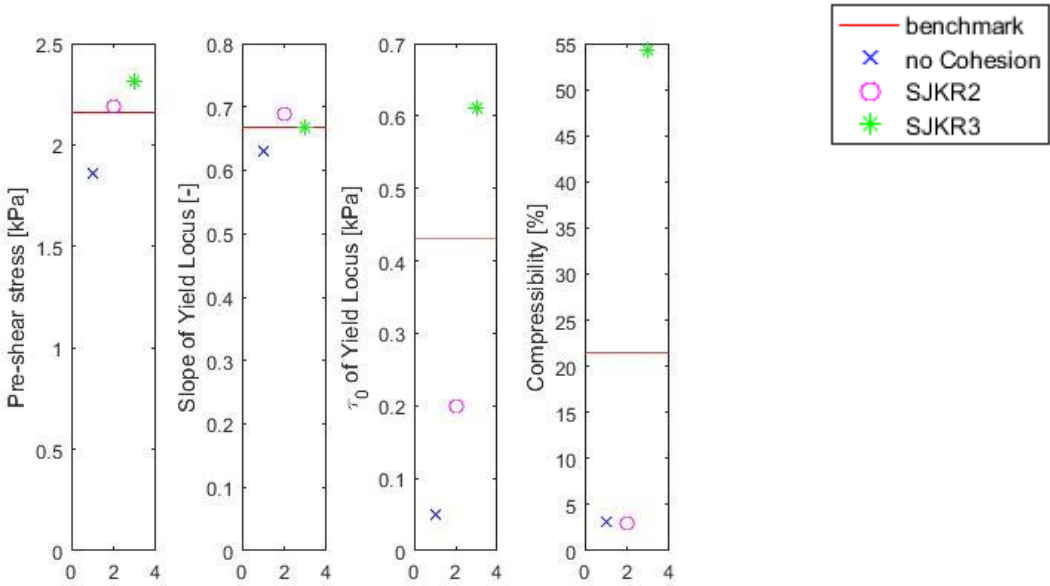


Figure 27: Comparison of the flow behavior of different cohesion models to the flow behavior of Lactohale 200 used as benchmark

It can be seen that the applicability of the SJKR2 cohesion model ends with moderate cohesive powders. Therefore, only the SJKR3 cohesion model is used to predict the flow behavior of a strong cohesive powder. Lactohale 220 is used as benchmark. Figure 28 show a strong cohesive flow behavior using the predicted simulation parameter. The accuracy of the predicted flow behavior is very good considering that the description of strong cohesive powders is not possible using the existing cohesion model. The modification enables a high compressibility as well as a high intercept of the yield locus. Only the slope of the yield locus is too low.

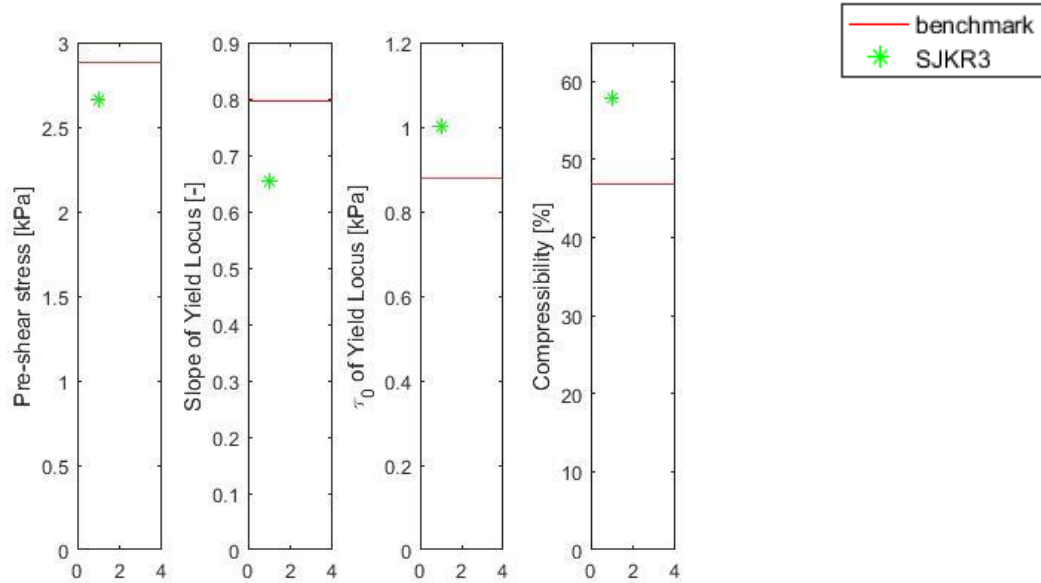


Figure 28: Comparison of the flow behavior of the SJKR3 cohesion models to the flow behavior of Lactohale 220 used as benchmark

Without a cohesion model, free flowing powders like Lactohale 100 can be described in a very good accuracy. The existing SJKR2 cohesion model allow to describe flow behavior of moderate cohesive powders like Lactohale 200. The modified SJKR3 cohesion models allows flow behaviors of strong cohesive powders like Lactohale 220. But the prediction shows, that the SJKR3 cohesion model is not physical. The influencing factors for the Yield Locus are interacting. A higher intercept of the yield locus results a lower slope. Therefore the Lactohale 220 cannot be described exactly, but sufficient accurate.

## ***5. Conclusions and Outlook***

The proposed calibration method is a useful tool to estimate appropriate simulation parameters. The precision of prediction is sufficient in the calibrated parameter range. The interaction of different simulation parameters complicates the prediction, especially for strong cohesive powders. The LIGGGHTS® built-in SJKR2 cohesion model is not capable of describing strong cohesive powder flow. Dense initial powder beds disable high compressibilities. High intercepts of the yield locus are also not possible. The modification of the SJKR2 cohesion model by adding an initial cohesion force improves the model and description of cohesive powder flows is enabled. Due to the modification of the SJKR3 model the capability of description of free flowing powders is reduced. The remaining introduced cohesion models (see 2.2) cannot be tested at this status of implementation, because of the difficulty of implementation of history based contact models.

Future work will be the implementation and testing of the remaining history based cohesion models. For the used cohesion models, a dimensionless overlap can be used to calculate the Young's modulus. As well as to test the applicability of the calibration method using other contact models. Another interesting contact model is the Luding model (Luding, 2008). The difference to the used Hertz model is the calculation of one contact force, including the cohesion and not a calculation of different force which are summed up. This thesis shows the possibilities of the calibration method. To exhaust the whole potential, new testing methods must be introduced and implemented. Every process is influenced from different types of flow behavior and the used testing methods must be chosen on a case-by-case basis.

## 6. References

- , R. B., Ketterhagen, W. R., & Hancock, B. C. (2010). Discrete element simulation study of a Freeman powder rheometer. *Chemical Engineering Science*, 65(21), 5747–5756. <https://doi.org/10.1016/j.ces.2010.04.002>
- Alizadeh, E., Bertrand, F., & Chaouki, J. (2014). Discrete element simulation of particle mixing and segregation in a tetrapodal blender. *Computers and Chemical Engineering*, 64, 1–12. <https://doi.org/10.1016/j.compchemeng.2013.12.009>
- Cleary, P. W., & Sawley, M. L. (2002). DEM modelling of industrial granular flows: 3D case studies and the effect of particle shape on hopper discharge. *Applied Mathematical Modelling*, 26(2), 89–111. [https://doi.org/10.1016/S0307-904X\(01\)00050-6](https://doi.org/10.1016/S0307-904X(01)00050-6)
- Cundall, P. A., & Strack, O. D. L. (1979a). A discrete numerical model for granular assemblies. *Geotechnique*. <https://doi.org/10.1680/geot.1979.29.1.47>
- Cundall, P. A., & Strack, O. D. L. (1979b). A discrete numerical model for granular assemblies. *Géotechnique*. <https://doi.org/10.1680/geot.1979.29.1.47>
- Fisher, R. A. (1936). The Design of Experiments. *The American Mathematical Monthly*, 43(3), 180. <https://doi.org/10.2307/2300364>
- Freeman, R. (2007). Measuring the flow properties of consolidated, conditioned and aerated powders - A comparative study using a powder rheometer and a rotational shear cell. *Powder Technology*, 174(1–2), 25–33. <https://doi.org/10.1016/j.powtec.2006.10.016>
- Furukawa, R., Shiosaka, Y., Kadota, K., Takagaki, K., Noguchi, T., Shimosaka, A., & Shirakawa, Y. (2016). Size-induced segregation during pharmaceutical particle die filling assessed by response surface methodology using discrete element method. *Journal of Drug Delivery Science and Technology*, 35, 284–293. <https://doi.org/10.1016/j.jddst.2016.08.004>
- Hamaker, H. C. (1937). The London--van der Waals Attraction between spherical particles. *Physica*, 4(10), 1058.
- Kloss, C. (2016). LIGGGHTS(R)-PUBLIC Documentation, Version 3.X.

- Kloss, C., Goniva, C., Hager, A., Amberger, S., & Pirker, S. (2012). Models , algorithms and validation for opensource DEM and CFD-DEM. *Pcfd*, 12, 140–152. <https://doi.org/10.1504/PCFD.2012.047457>
- Loidolt, P., Madlmeir, S., & Khinast, J. G. (2017). Mechanistic modeling of a capsule filling process. *International Journal of Pharmaceutics*, 532(1), 47–54. <https://doi.org/10.1016/j.ijpharm.2017.08.125>
- Luding, S. (2008). Cohesive, frictional powders: Contact models for tension. *Granular Matter*, 10(4), 235–246. <https://doi.org/10.1007/s10035-008-0099-x>
- Owen, P. J., & Cleary, P. W. (2009). Prediction of screw conveyor performance using the Discrete Element Method (DEM). *Powder Technology*, 193(3), 274–288. <https://doi.org/10.1016/j.powtec.2009.03.012>
- Pantaleev, S., Yordanova, S., Janda, A., Marigo, M., & Ooi, J. Y. (2017). An experimentally validated DEM study of powder mixing in a paddle blade mixer. *Powder Technology*, 311, 287–302. <https://doi.org/10.1016/j.powtec.2016.12.053>
- Pei, C., & Elliott, J. A. (2017). Asymptotic limits on tablet coating variability based on cap-to-band thickness distributions: A discrete element model (DEM) study. *Chemical Engineering Science*, 172, 286–296. <https://doi.org/10.1016/j.ces.2017.06.029>
- Wilkinson, S. K., Turnbull, S. A., Yan, Z., Stitt, E. H., & Marigo, M. (2017). A parametric evaluation of powder flowability using a Freeman rheometer through statistical and sensitivity analysis : A discrete element method ( DEM ) study. *Computers and Chemical Engineering*, 97, 161–174. <https://doi.org/10.1016/j.compchemeng.2016.11.034>

## 7. Table of Figures

Figure 1: Cohesion Force over Overlap Area for SJKR2 model.....	5
Figure 2: Cohesion Force over Overlap Area for SJKR3 model.....	6
Figure 3: Cohesion Force over Overlap for SJKR-HYS model.....	7
Figure 4: Distance function over Hertzian force for the HVDW model.....	8
Figure 5: Cohesion force over Hertzian force for HSF model.....	9
Figure 6: Filled vessel at FT4 experiment (left) and DEM simulation (right).....	10
Figure 7: Particle size distribution .....	11
Figure 8: Plot of the Yield Locus fitted through the Yield points in the $\sigma$ - $\tau$ diagram .....	12
Figure 9: Shear cell module of the FT4 rheometer (left) and model of the rotational shear test (right) .....	13
Figure 10: Compressibility over Normal stress .....	13
Figure 11: Compressibility module of the FT4 rheometer (left) and simulation of the compressibility testing (right) .....	14
Figure 12: $\sigma$ - $\tau$ diagram for the Wall Friction experiment.....	15
Figure 13: Simulation of the wall friction testing and stress over time diagram.....	15
Figure 14: DoE example for two factors. Schematic view for the main effect of factor 1 (left) and factor 2 (right).....	16
Figure 15: Main effects plot for a DoE with two factors.....	17
Figure 16: Factors and responses for the DEM simulations of the standard experiments.....	18
Figure 17: Main effects plot for the Pre-Shear Stress using the SJKR2 cohesion model.....	22
Figure 18: Main effects plot for the Slope of the Yield Locus using the SJKR2 cohesion model .....	22
Figure 19: Main effects plot for the $\tau_0$ of the Yield Locus using the SJKR2 cohesion model....	23
Figure 20: Main effects plot for the compressibility using the SJKR2 cohesion model .....	24
Figure 21: Main effects plot for the slope of the yield locus using the SJKR3 cohesion model	26
Figure 22: Main effects plot for the $\tau_0$ of the Yield Locus using the SJKR3 cohesion model....	27
Figure 23: Main effects plot for the compressibility using the SJKR3 cohesion model .....	27
Figure 24: Main effects plot for the Pre-Shear Stress using the HVDW cohesion model.....	31
Figure 25: Main effects plot for the compressibility using the HVDW cohesion model.....	31
Figure 26: Comparison of the flow behavior of different cohesion models to the flow behavior of Lactohale 100 used as benchmark .....	38

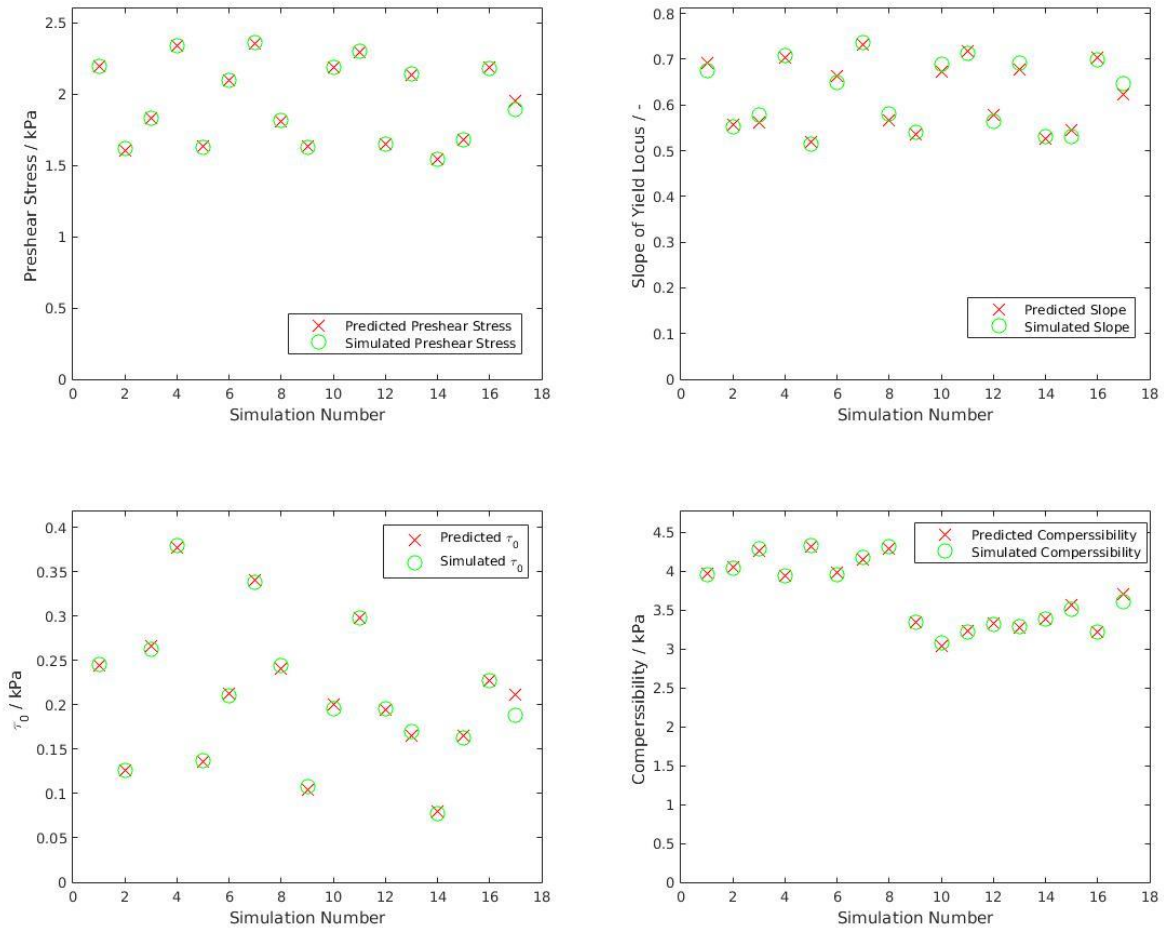
Figure 27: Comparison of the flow behavior of different cohesion models to the flow behavior of Lactohale 200 used as benchmark .....	39
Figure 28: Comparison of the flow behavior of the SJKR3 cohesion models to the flow behavior of Lactohale 220 used as benchmark .....	40

## 8. Appendix

### *SJKR2 cohesion model*

Sim #	1	2	3	4	5	6	7	8	9	10	11	12	13	14	15	16
Young	-1	-1	-1	-1	-1	-1	-1	-1	1	1	1	1	1	1	1	1
dia	-1	-1	-1	-1	1	1	1	1	-1	-1	-1	-1	1	1	1	1
cohE	-1	-1	1	1	-1	-1	1	1	-1	-1	1	1	-1	-1	1	1
mu	1	-1	-1	1	-1	1	1	-1	-1	1	1	-1	1	-1	-1	1
e	-1	1	-1	1	-1	1	-1	1	-1	1	-1	1	-1	1	-1	1

A 1: DOE design for calibration using the SJKR2 cohesion model

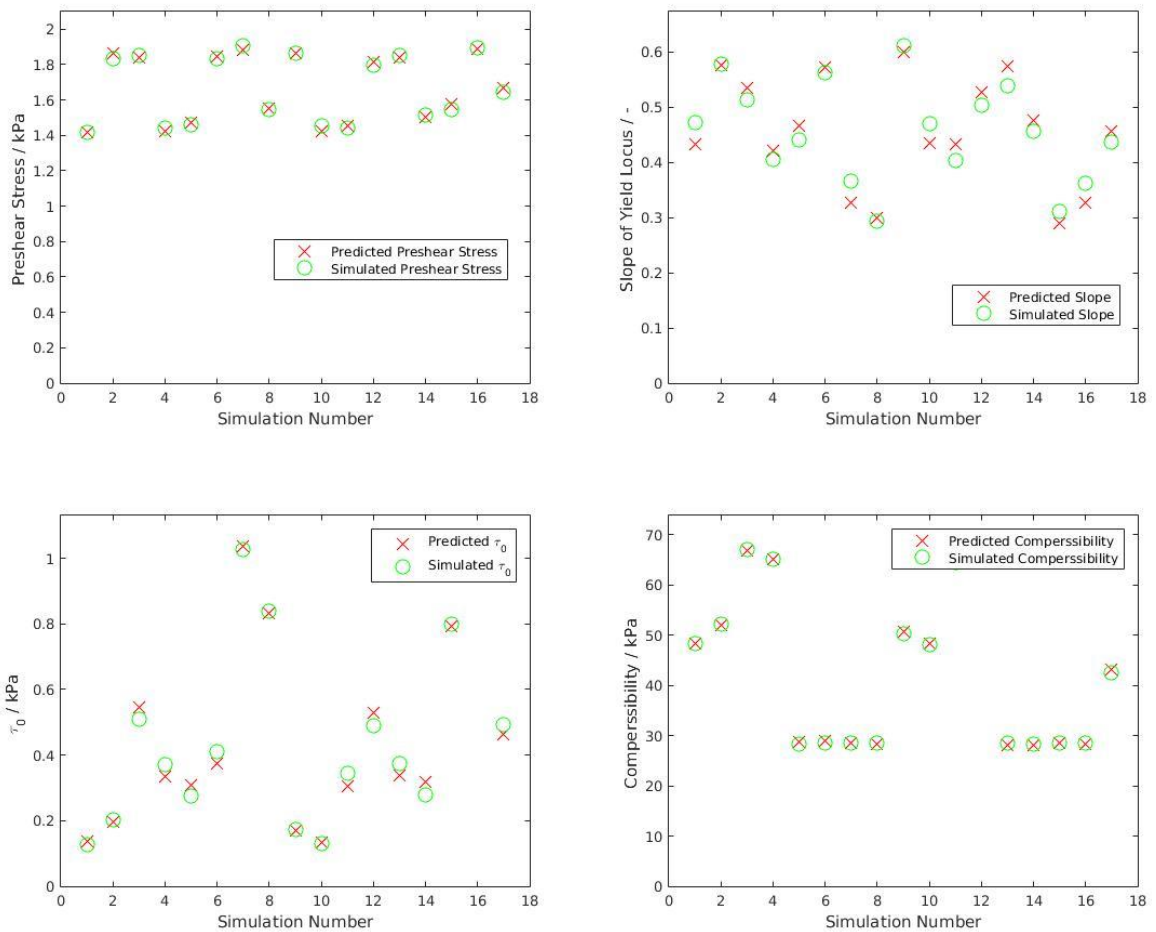


A 2: Results and Predicted Values for the different calibration methods using the SJKR2 cohesion model

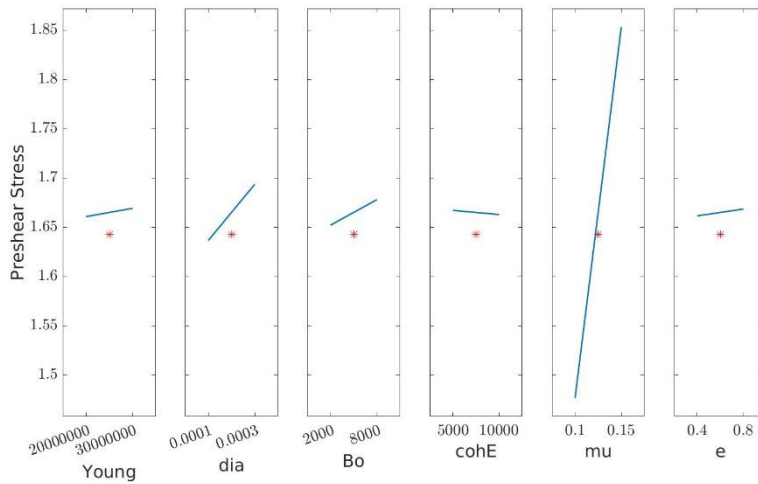
*SJKR3 cohesion model*

Sim #	1	2	3	4	5	6	7	8	9	10	11	12	13	14	15	16
Young	-1	-1	-1	-1	-1	-1	-1	-1	1	1	1	1	1	1	1	1
dia	-1	-1	-1	-1	1	1	1	1	-1	-1	-1	-1	1	1	1	1
Bo	-1	-1	1	1	-1	-1	1	1	-1	-1	1	1	-1	-1	1	1
cohE	1	-1	-1	1	-1	1	1	-1	-1	1	1	-1	1	-1	-1	1
mu	-1	1	1	-1	-1	1	1	-1	1	-1	-1	1	1	-1	-1	1
e	-1	1	-1	1	1	-1	1	-1	1	-1	1	-1	-1	1	-1	1

A 3: DOE design for calibration using the SJKR3 cohesion model



A 4: Results and Predicted Values for the different calibration methods using the SJKR3 cohesion model

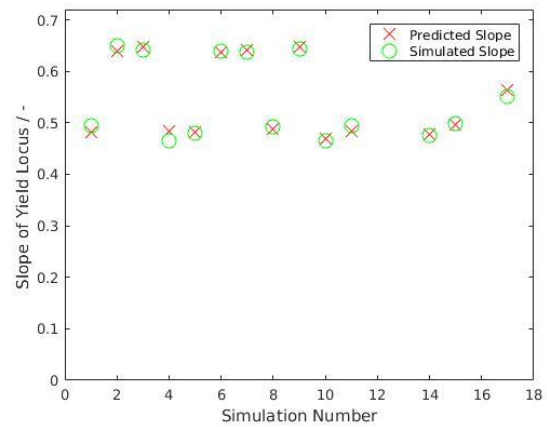
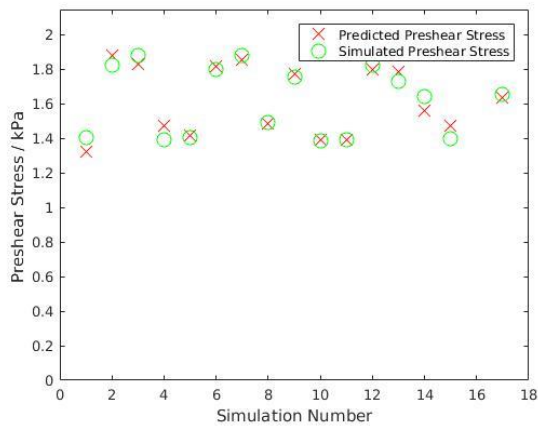


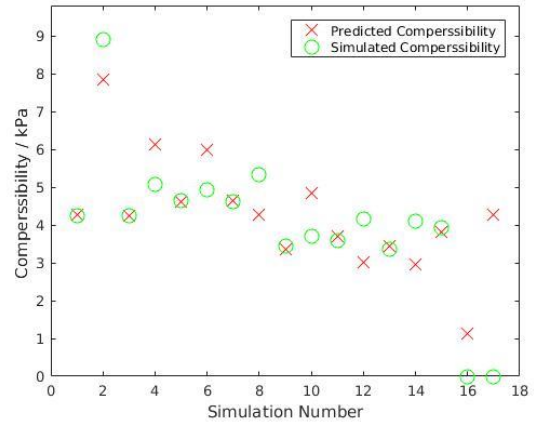
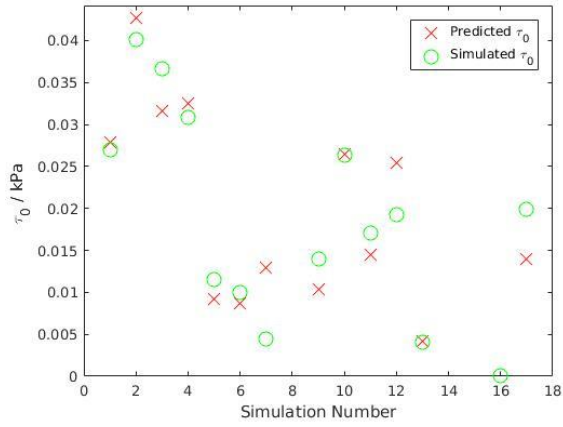
A 5: Main effects plot for the pre-shear stress using the SJKR3 cohesion model

*SJKR Hysteresis cohesion model*

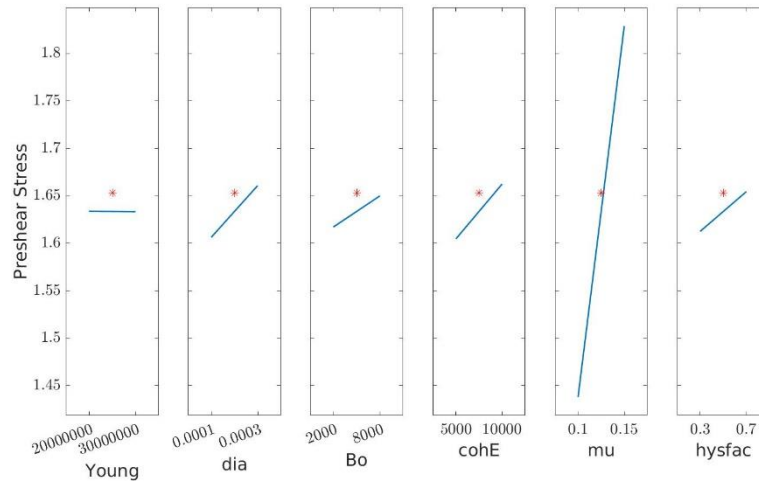
Sim #	1	2	3	4	5	6	7	8	9	10	11	12	13	14	15	16
<b>Young</b>	-1	-1	-1	-1	-1	-1	-1	-1	1	1	1	1	1	1	1	1
<b>dia</b>	-1	-1	-1	-1	1	1	1	1	-1	-1	-1	-1	1	1	1	1
<b>Bo</b>	-1	-1	1	1	-1	-1	1	1	-1	-1	1	1	-1	-1	1	1
<b>cohE</b>	1	-1	-1	1	-1	1	1	-1	-1	1	1	-1	1	-1	-1	1
<b>mu</b>	-1	1	1	-1	-1	1	1	-1	1	-1	-1	1	1	-1	-1	1
<b>hysfac</b>	-1	1	-1	1	1	-1	1	-1	1	-1	1	-1	-1	1	-1	1

A 6: DOE design for calibration using the SJKR Hysteresis cohesion model

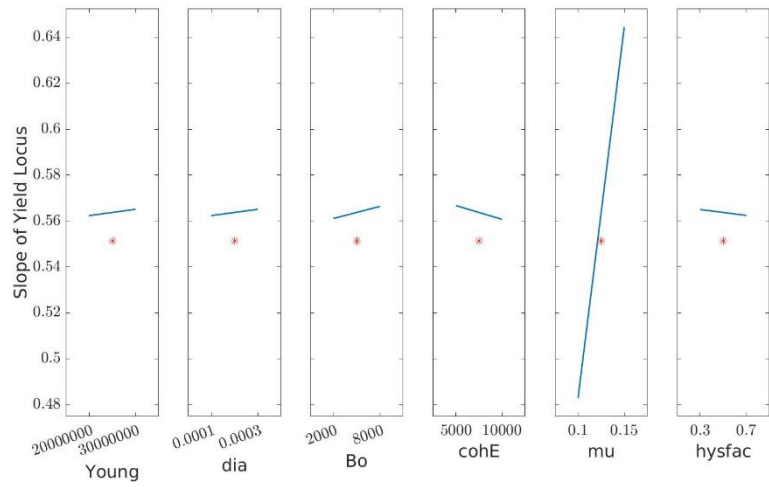




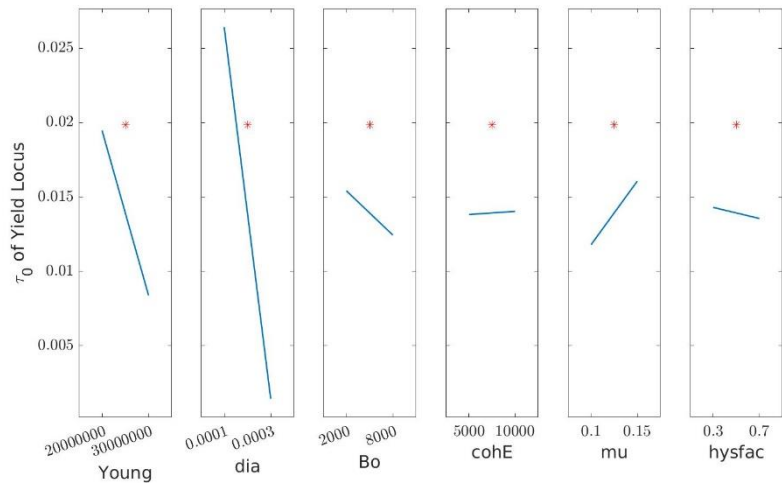
A 7: Results and Predicted Values for the different calibration methods using the SJKR Hysteresis cohesion model



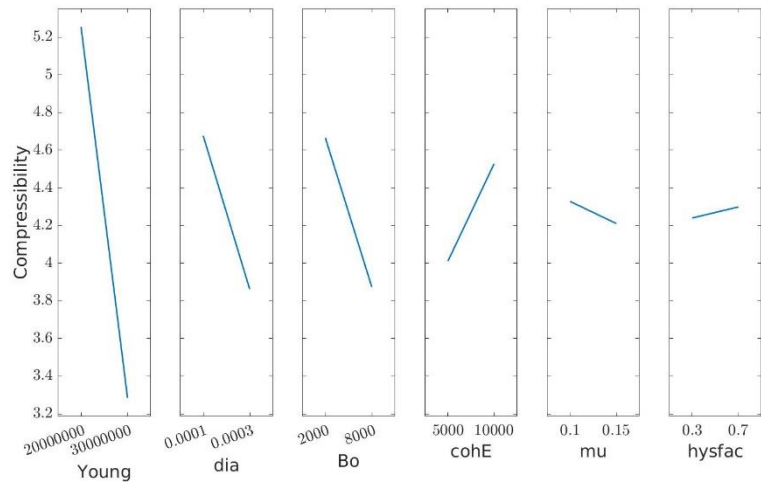
A 8: Main effects plot for the pre-shear stress using the SJKR Hysteresis cohesion model



**A 9: Main effects plot for the slope of the yield locus using the SJKR Hysteresis cohesion model**



**A 10: Main effects plot for the intercept of the yield locus using the SJKR Hysteresis cohesion model**

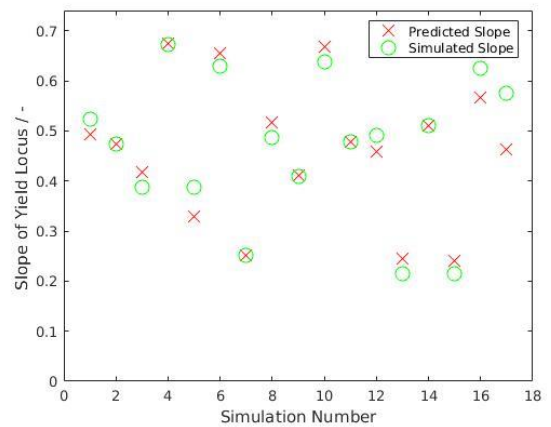
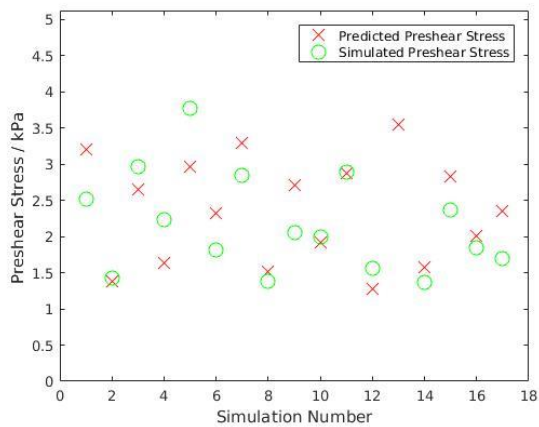


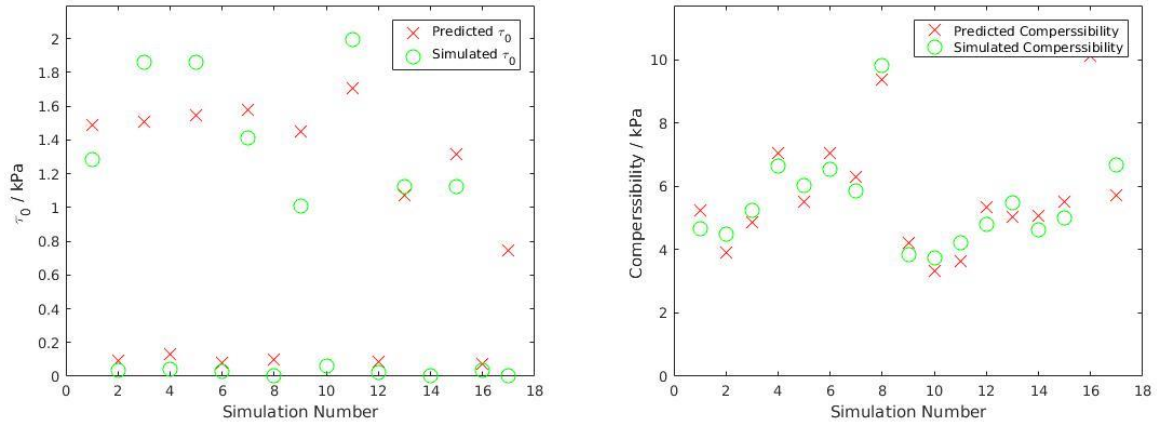
A 11: Main effects plot for the compressibility using the SJKR Hysteresis cohesion model

*HVDW cohesion model*

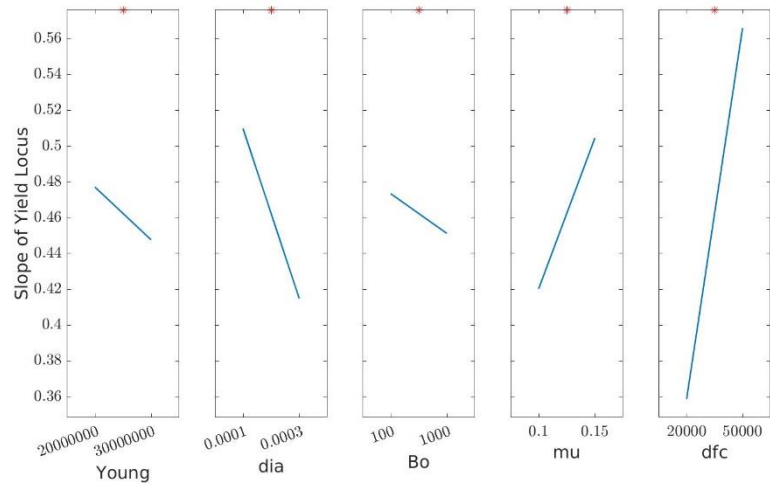
Sim #	1	2	3	4	5	6	7	8	9	10	11	12	13	14	15	16
Young	-1	-1	-1	-1	-1	-1	-1	-1	1	1	1	1	1	1	1	1
dia	-1	-1	-1	-1	1	1	1	1	-1	-1	-1	-1	1	1	1	1
Bo	-1	-1	1	1	-1	-1	1	1	-1	-1	1	1	-1	-1	1	1
mu	1	-1	-1	1	-1	1	1	-1	-1	1	1	-1	1	-1	-1	1
dfc	-1	1	-1	1	-1	1	-1	1	-1	1	-1	1	-1	1	-1	1

A 12: DOE design for calibration using the HVDW cohesion model

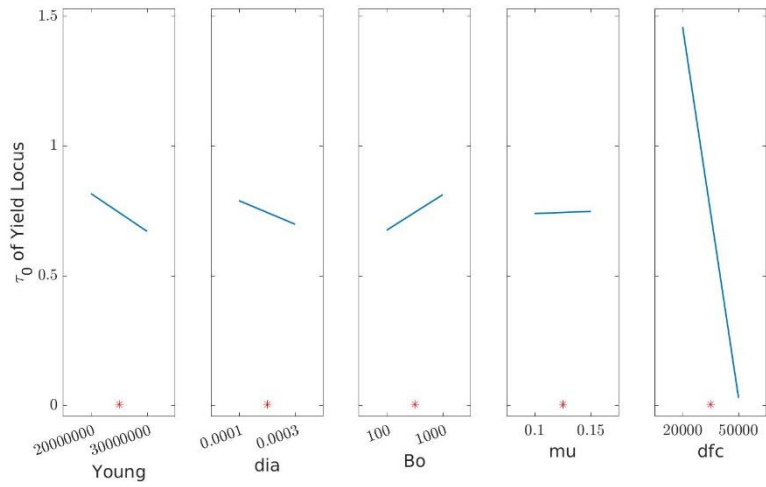




A 13: Results and Predicted Values for the different calibration methods using the HVDW cohesion model



A 14: Main effects plot for the slope of the yield locus using the HVDW cohesion model

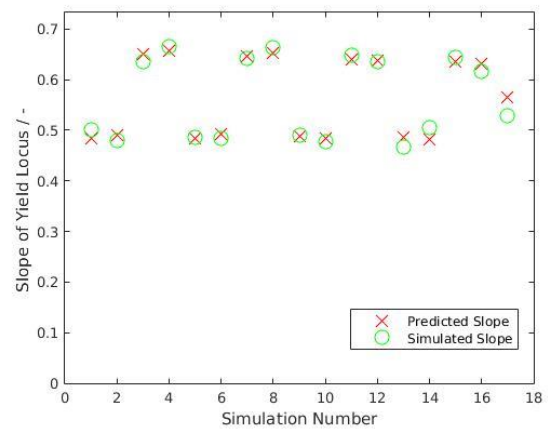
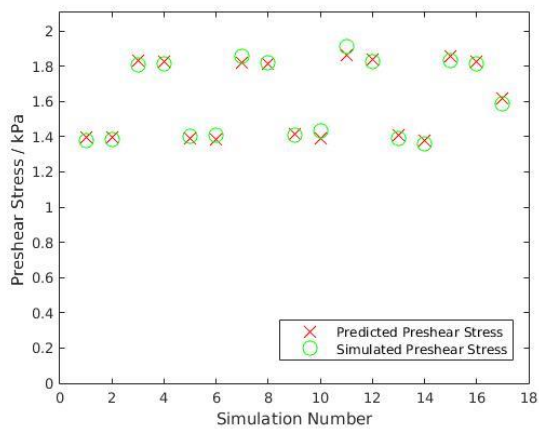


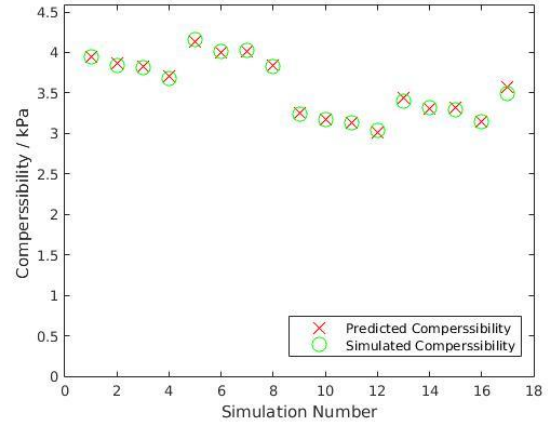
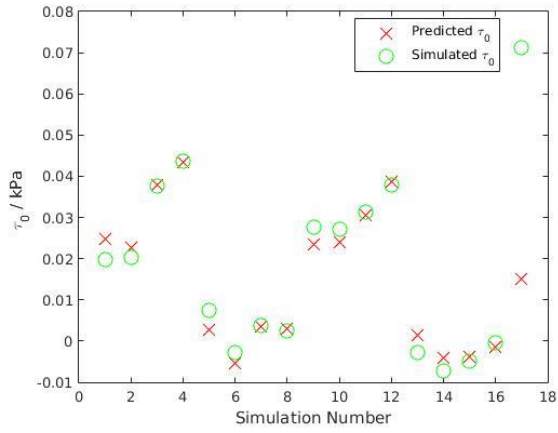
A 15: Main effects plot for the intercept of the yield locus using the HVDW cohesion model

*No cohesion model*

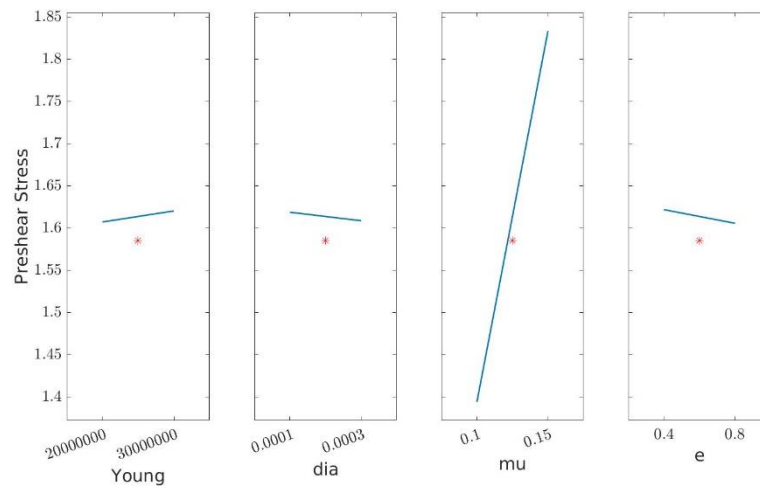
Sim #	1	2	3	4	5	6	7	8	9	10	11	12	13	14	15	16
Young	-1	-1	-1	-1	-1	-1	-1	-1	1	1	1	1	1	1	1	1
dia	-1	-1	-1	-1	1	1	1	1	-1	-1	-1	-1	1	1	1	1
mu	-1	-1	1	1	-1	-1	1	1	-1	-1	1	1	-1	-1	1	1
e	-1	1	-1	1	-1	1	-1	1	-1	1	-1	1	-1	1	-1	1

A 16: DOE design for the calibration without a cohesion model

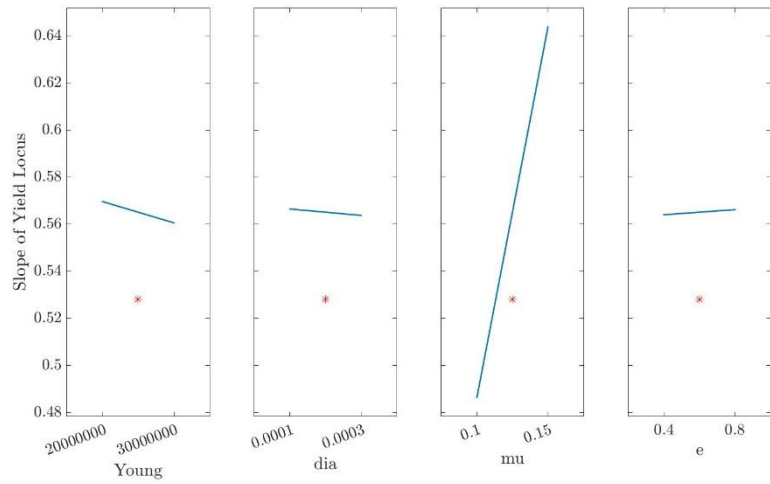




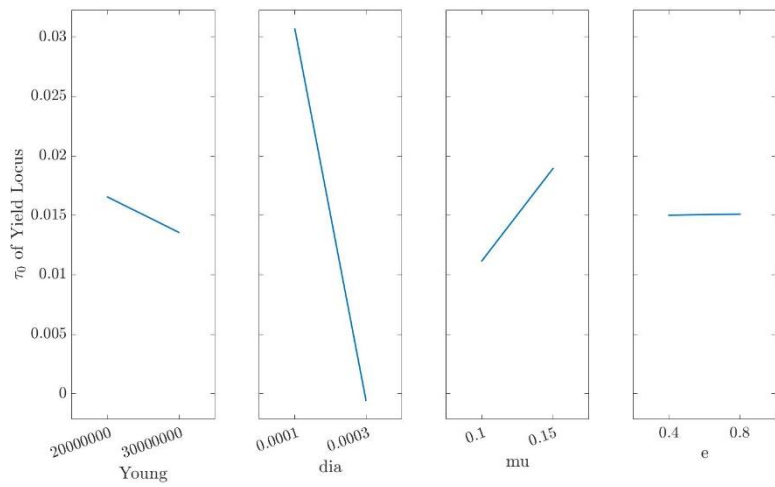
A 17: Results and Predicted Values for the different calibration methods without a cohesion model



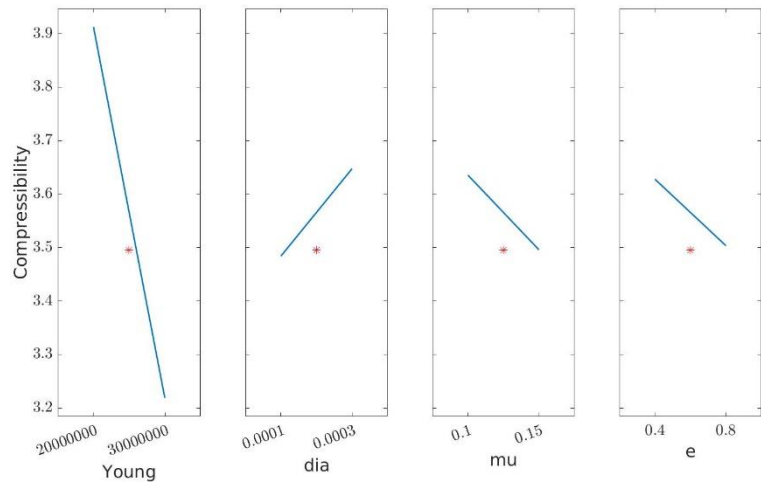
A 18: Main effects plot of the pre-shear stress without a cohesion model



**A 19: Main effects plot of the slope of the yield locus without a cohesion model**



**A 20: Main effects plot of the  $\tau_0$  of the yield locus without a cohesion model**



A 21: Main effects plot of the compressibility without a cohesion model